

MASTER 2 INTERSHIP REPORT

by

Antoine Rocher

MODELLING NON-LINEAR EFFECTS OF REDSHIFT-SPACE DISTORTIONS INDUCED BY GALAXY PECULIAR VELOCITIES

Advisor: Sylvain de la Torre

Defense june 21st, 2019

at CRAL, Centre de Recherche d'Astrophysique de Lyon

Abstract

Understanding the formation and evolution of large-scale structure is a central problem in cosmology and enables precise tests of General Relativity on cosmological scales and constraints on dark energy. An essential ingredient is to study the effect of peculiar velocities of galaxy. They induced distortion in the pattern of galaxy redshift surveys that we can use to provide some measurements on the growth of structure in the universe. In this work we describe the Convolution Lagrangian Perturbation Theory predictions of real-space clustering and velocity statistics in the Gaussian streaming model of Reid & White (2011) to obtain predictions for the multipoles and the two-points correlation function. We implement a C code for both models and compare predictions with numerical cosmological N-body simulations.

*Laboratoire d'Astrophysique de Marseille
Pôle de l'Étoile – Site de Château-Gombert
38, rue Frédéric Joliot-Curie
Marseille*

Contents

1	Introduction	1
2	Cosmological context	1
2.1	The expansion of the Universe	1
2.2	The standard model of cosmology	2
3	The Large Scales Structures of the Universe	5
3.1	Eulerian linear perturbation theory and structure formation	5
3.2	Correlation function and Power Spectrum	7
4	Redshift-space distortions as probe of structure growth	9
4.1	Redshift-space distortions	9
4.2	Kaiser model of linear Redshift Space Distortion	11
4.3	Galaxy bias	13
5	Gaussian streaming model	14
6	Convolution Lagrangian Perturbation Theory	16
6.1	Lagrangian Perturbation Theory	16
6.2	Biased Tracer in LPT	16
6.3	Redshift space	17
6.4	CLPT predictions	17
7	Code/Numerical analysis	19
7.1	Code Process	19
7.2	Code results	21
8	Simulation	23
8.1	Comparison Simulation-GS+CLPT model	23
9	Conclusion	25
A	CLPT functions	26

1 Introduction

Some of the most important mysteries in modern cosmology are the nature of dark energy and dark matter. The standard model of cosmology is built upon an assumption of isotropy and homogeneity of the Universe. Indeed, observations revealed that galaxies are not randomly distributed in the Universe but form a web-like structure on scales of hundreds of megaparsecs. Observations of the large-scale structure of the Universe play an important role in investigations of the origin of cosmic acceleration. One of the most important cosmological probes to understand structure formation and cosmic acceleration is the growth of the large-scale structure of the Universe. This growth is driven by the competition between gravitational attraction and the expansion of space-time, allowing us to test both the nature of gravity and the expansion history of the Universe. Despite the fact that galaxy light does not faithfully trace the entire matter in the Universe, galaxies are acting as test particles within the cosmological flow of matter. Therefore, galaxy peculiar velocities carry an imprint of the rate at which the large-scale structure grows and allows us to both probe dark energy and test General Relativity on the largest scales. Peculiar galaxy motions along the line of sight (los) generate the leading corrections and give rise to the redshift-space distortions (RSD). RSD can evaluate galaxy motion in redshift galaxy surveys and therefore, are used as tool to probe the growth of structure in the universe. During the last decades, analytical models have been developed to understand RSD effect. The first linear approach was made by Kaiser in 1987. Afterwards, several approaches have been pursued to improve our understanding of RSD, including perturbation approaches. In this work we study how we can extract cosmological information from RSD. We focus our study on the Gaussian Streaming model of Peebles (1980), using a Lagrangian perturbation approach to describe the effect of RSD. We implement a C code for this model and compare the prediction of this model with numerical simulation. The outline of this work is as follow. In the first part we introduce important concepts to describe the current cosmological model. The second part focuses on the description of the Large Scale structures of the universe and give a theoretical description of the structure formation in the universe. Section 4 describes the theory of redshift space distortion effect. Section 5 we present the gaussian streaming model of redshift space distortion that we apply in Section 6 to the Convolution Lagrangian Perturbation Theory for redshift space distortion. In section 7, we present our implementation in a C codes of both previous models. In Section 7, we compare models with numerical N-body simulations.

2 Cosmological context

2.1 The expansion of the Universe

Cosmology consists in studying the origin, the content, and the evolution of the Universe. During the XX^{th} century, scientists have tried to explain the shape and the structure of our universe. Pioneering cosmological theories have been developed and first detailed extragalactic observations of galaxies have been conducted by astronomers. In 1910, Vesto Slipher showed the existence of a spectral shift between the observed galaxy spectral features and their wavelengths at rest, systematically towards the red side (higher wavelengths) of the spectra. In the late 1920s, Edwin Hubble evidenced the recession velocity of nearby galaxies, which then lead with the work of Georges Lemaître to the discovery of the expansion of the Universe: galaxies tend to move away from each other proportionally to the distance between them. This today known as the **Lemaître-Hubble law** :

$$v = H_0 \times D, \tag{1}$$

where H_0 is the Hubble constant in $\text{km s}^{-1} \text{Mpc}^{-1}$ and D the proper distance of the galaxy in megaparsec (Mpc)*. This relation is interpreted as an evidence of universal's expansion. The Universe itself undergoes a spatial expansion and objects follow it. This phenomenon is commonly referred to as the Hubble flow. The Hubble constant H_0 refers to the expansion rate of the universe today. Its value is usually written:

$$H_0 = 100 h \text{ km s}^{-1} \text{Mpc}^{-1} \quad (2)$$

Where h is the reduced Hubble's constant. Several determinations of H_0 have been done and current most accurate measurements have been obtained from the study of the luminosity of type-1a supernovae and Cepheids in the nearby Universe, and the Cosmic Microwave Background (CMB) anisotropy. While former measurements give $h = 0.72$ ((Riess et al. 2016)), Planck satellite CMB observations derive a lower value of $h = 0.67$ (Planck Collaboration et al. 2016). The statistical uncertainty on these measurements are rather low and the origin of this discrepancy is not yet fully understood.

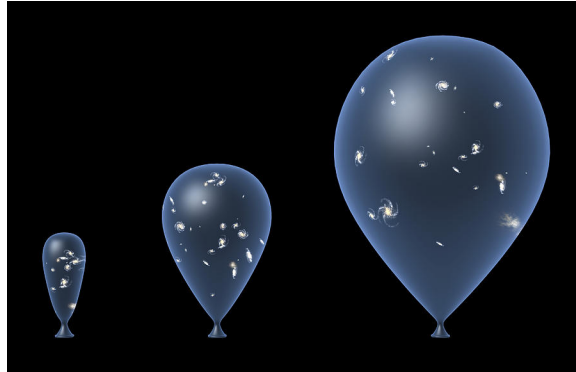


Figure 1: Schematic view of the expansion of the Universe

The expansion of the Universe introduces a spectral shift between the observed wavelengths λ_{obs} and those at rest λ_R . This can be understood as an analogue of the Doppler effect:

$$z = \frac{\lambda_{obs}}{\lambda_R} - 1, \quad (3)$$

where z is the *redshift*. However, this is not a Doppler shift, only photons are moving. Photon's wavelengths shift with the expansion of the Universe. To avoid the fact that the Universe is expanding, we commonly use cosmological comoving distances that correspond to a distance that does not change in time due to the expansion of space.

2.2 The standard model of cosmology

The standard cosmological model is based on the **Cosmological Principle**. It states that the Universe is homogeneous and isotropic at very large scales. A fundamental principle of this model is that the dynamics of the Universe is governed by Einstein theory of General Relativity (GR). It is a theory of gravity in which the gravity is not considered as a force, but as a manifestation of the curvature of space-time. The last decades have seen the building of the standard or concordance model of cosmology, called Λ -CDM (Cold Dark Matter). In this model, the Universe emerges

*1 Mpc $\approx 3.1 \times 10^{22} \text{m}$

out of a "Big-Bang" (BB) initial stage, 13.8 billion years ago, and expands through an unknown cosmological component Λ . It represents the cosmological constant, which is currently associated to vacuum energy or dark energy and is used to explain the contemporary accelerating expansion of space against the attractive effects of gravity. In Λ -CDM model, the universe is dominated by the dark energy Ω_Λ and composed of 2 types of matter : baryonic matter and cold Dark Matter (DM). The former relates to usual matter which we can observe while the latter only interacts gravitationally with the former. There are several observational evidences of DM such as the gravitational lensing or rotation curves of galaxies. A homogeneous and isotropic universe can be described using the Friedmann-Lemaître-Robertson-Walker (FLRW) metric :

$$ds^2 = c^2 dt^2 - a^2(t) \left[\frac{dr^2}{1 - kr^2} + r^2 d\Omega^2 \right] \quad (4)$$

where $a(t)$ is the scale factor and $k = 0, -1, +1$ describes the local curvature of space (flat, hyperbolic or spherical). The cosmic expansion rate at any time t is therefore characterised by the Hubble parameter $H = \dot{a}/a$. In the concordance model Λ -CDM, the universe is considered to be flat $k = 0$. The dynamics of the universe $R(t)$ is described by resolving the Einstein equations of General Relativity :

$$R_{\mu\nu} - \frac{1}{2} g_{\mu\nu} R = 8\pi G T_{\mu\nu} + \Lambda g_{\mu\nu} \quad (5)$$

Where $R^{\mu\nu}$ is the Ricci tensor which completely defines the space-time deformations. R is the Ricci scalar as $R = g_{\mu\nu} R^{\mu\nu}$ and $T_{\mu\nu}$ is the stress-energy tensor. Solving Eq.5 for a FLRW metric yield to the famous Friedmann equation :

$$\begin{cases} \left(\frac{\dot{a}}{a} \right)^2 = 8\pi G \rho - \frac{a}{k^2} \\ \frac{\ddot{a}}{a} = -\frac{4\pi G}{3} (\rho + 3P) \end{cases} \quad (6)$$

With ρ and P the density and pressure content of the universe. These equations describe the relationship between the temporal evolution of the scale factor $a(t)$ and the physical properties of the universe, its geometry and energy content. The total energy density of the Universe, as a sum of several component : matter ρ_m , radiation ρ_r , dark energy ρ_Λ and curvature ρ_k . From Eq.6 we can define a critical density for a homogeneous Universe ($k = 0$):

$$\rho_c = \frac{3H^2}{8\pi G} \quad (7)$$

which defines the energy density where the universe will stop its expansion at an infinite time. A common quantity used in cosmology is the reduced density $\Omega_i = \rho_i/\rho_c$ and first Friedmann equation reads :

$$\Omega_m + \Omega_r + \Omega_\Lambda + \Omega_k = 1 \quad (8)$$

Therefore we can rewrite the temporal evolution of the scale factor as a function of the energy content of the universe today from Eq. 6 :

$$H(z) = H_0 \left(\Omega_r (1+z)^4 + \Omega_m (1+z)^3 + \Omega_k (1+z)^2 + \Omega_\Lambda \right)^{1/2} \quad (9)$$

. For Λ -CDM model, observations give an estimation for the composition of the universe today as $\Omega_r \approx 0.01\%$, $\Omega_M \approx 32\%$ and $\Omega_\Lambda \approx 68\%$ (Planck Collaboration et al. 2016).

During the last century, main observational evidences of the hot "Big-Bang" theory have been:

- **Cosmological Redshift** : Lemaître-Hubble law describes the fact that galaxies move away from us at a velocity proportional to their distance. It is considered as the first observational evidence that the Universe is expanding.
- **Cosmic Microwave Background (CMB)** : Discovered by Penzias & Wilson (1965) in 1965, the CMB is a landmark evidence of the BB origin. When the universe was very young, all particles (proton, electron..) were condensed in a primordial plasma. The universe was so dense that the photons were always captured by hydrogen core which makes the universe opaque to radiation. After 380 000 years, the temperature of the universe goes below 3000 Kelvin, protons and electrons form neutral atoms as *recombination epoch* and photons start to travel freely through space. The temperature of the CMB decreases as the universe expand, and reaches $\sim 2.72K$ today.
- **Chemical abundance of primordial elements** During the first 3 seconds of the universe, there is the primordial nucleosynthesis phase where simple chemical elements (e.g. hydrogen (2H), helium (4He), lithium (7Li)) were synthesised. BB theory can predict the cosmic abundance of each one these elements, and observational measurements are consistent with this model (Burbidge et al. 1957).

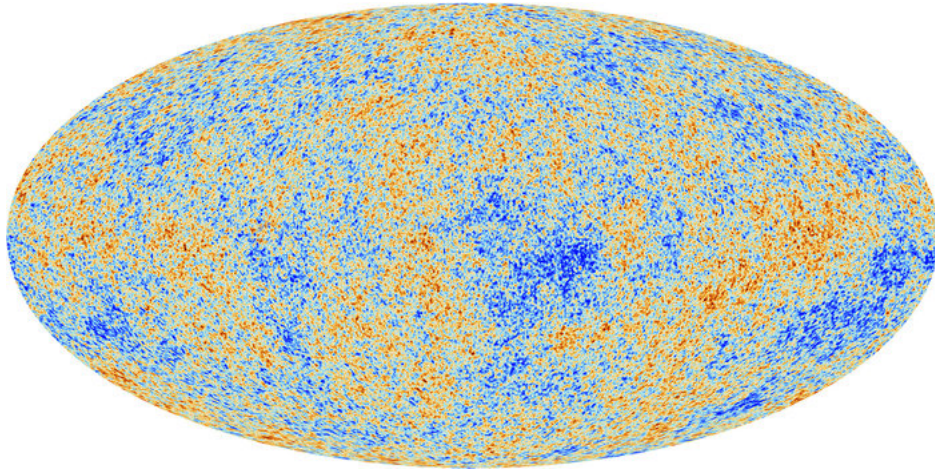
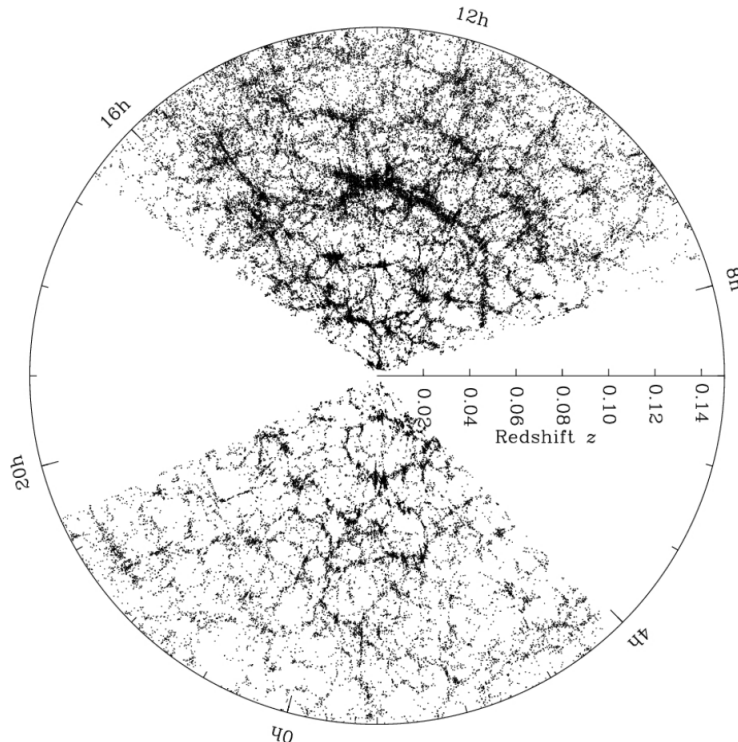


Figure 2: Cosmic Microwave Background temperature map measured by the Planck collaboration (Planck Collaboration et al. 2014)

The CMB (Figure 2) is an important observational evidences of the standard model. The first measurement of CMB shows a isotropic radiation a $T \approx 2.7K$, but recent measurement find temperature fluctuations $\Delta T \approx 10^{-5}K$. These fluctuations generate wiggles in the photon-matter plasma due to the competition between gravitational forces and radiative pressure. Theses wiggles are imprint in the power spectrum and are called Baryon Acoustic Oscillations(BAO). These temperature fluctuations give the initial conditions on what will become the Large-Scale Structures (LSS).

3 The Large Scales Structures of the Universe

The hypothesis of an homogeneous and isotropic universe can only be valid on extremely large scales. Indeed, large galaxy redshift surveys such as SDSS (Sloan Digital Sky Survey) provide a three-dimensional view of the large-scale structure of the universe. Figure 3 shows the large-scale structure (LSS) or **cosmic web**, a rich structure with a web-like pattern, containing knots with clusters or superclusters and filaments with long strands of galaxies and large empty regions on scales up to a few hundreds to thousands of Mpc. Galaxy redshift surveys are powerful cosmological tools for understanding the geometry and the dynamics of the Large Scale Structure of the Universe.



3.1 Eulerian linear perturbation theory and structure formation

The formation history of the LSS teaches us a lot of information about the content of the universe. In the standard paradigm of structure formation, today's large-scale structure is believed to originate from initial quantum fluctuations in the primordial plasma that leads to inhomogeneities in the CMB temperature map (Fig.2) and therefore in the matter density. Those initial density perturbations grow under the laws of gravity until the formation of galaxies and clusters. In the Eulerian linear perturbation theory, it is possible to describe the growth of a small amplitude density fluctuation through a second-order differential equation. This equation depends on the expansion rate $H(z)$, but also on the theory of gravity. From its solutions, we can define the linear growth rate of structure $f(z)$, which measures how rapidly structures assembled in the Universe as a function of cosmic time, or, equivalently, of redshift.

We consider the gravitational evolution of a pressureless fluid with no vorticity for the velocity field gives in a single flow regime, where the gravity dominates over the velocity dispersion of galaxies. This approximation allows one to study the first stages of gravitational instability at large scale ($> 50 h^{-1}$ Mpc) but breaks down as soon as shell-crossing occurs at small scale ($< 50 h^{-1}$ Mpc)

e.g. when non-linear structures like filaments and halos form. In this case, the dynamics of the cosmic fluid is described by the following closed system of three coupled equations : continuity equation (mass conversation), Euler equation of motion and Poisson equation (for the gravitational potential):

$$\begin{cases} \frac{d\rho}{dt} + \nabla \cdot (\rho \mathbf{u}) = 0 \\ \frac{d\mathbf{u}}{dt} + (\mathbf{u} \cdot \nabla) \mathbf{u} = -\nabla \Phi \\ \Delta \Phi = 4\pi G \rho \end{cases} \quad (10)$$

where \mathbf{u} is the velocity field, ρ the matter density and Φ the gravitational potential. This equation system can be rewrite as a function of the matter density contrast $\delta = \frac{\rho(\mathbf{r},t) - \bar{\rho}(t)}{\bar{\rho}(t)}$ and, using perturbations at linear order, leads to a second-order equation for the density contrast:

$$\ddot{\delta} + 2H\dot{\delta} - 4\pi G\bar{\rho}\delta = 0 \quad (11)$$

The Hubble drag $2H\dot{\delta}$ shows the attenuation of the growth of perturbations through cosmic expansion which is in competition with the gravitational term $\propto g\delta$. In the linear approach, the shape of the fluctuation in the density field is constant with a factor $D(t)$ and independent of the position or the scale. The growth of fluctuations in time can be obtained by solving Eq. 11. That has typically one growing $D_+(t)$ and one decaying $D_-(t)$ mode :

$$\delta(\mathbf{x}, t) = D_+(t)\delta_+(\mathbf{x}, 0) + D_-(t)\delta_-(\mathbf{x}, 0) \quad (12)$$

Then, keeping only the growing mode, we can rewrite $\dot{\delta}$ as a function of $\delta(\mathbf{x}, t)$:

$$\dot{\delta} = H \frac{\partial \log D_+(t)}{\partial \log a} \delta(\mathbf{x}, t) \quad (13)$$

Finally, we introduce the linear growth rate f :

$$\dot{\delta} = Hf\delta(\mathbf{x}, t), \text{ with } f(z) = \frac{\partial \log D_+(t)}{\partial \log a(t)} \quad (14)$$

and the continuity equation becomes :

$$\nabla \mathbf{u} = -aHf\delta \quad (15)$$

The structure growth is currently slower in a Λ -CDM universe than before (when the matter density was the dominant energy component in the universe) because the expansion rate and then the hubble drag is bigger. Consequently current observe fluctuations should be greater in the past. The growth factor $f(z)$ essentially depends on the value of the mass density parameter Ω_M at the given epoch. For a flat universe in which the total density in matter and dark energy is $\Omega_\Lambda + \Omega_M = 1$ this dependence can be derive from GR. and we obtain $f(z) \approx \Omega_M(z)^{0.55}$ (Nesseris & Perivolaropoulos 2008). However, this is not valid if the observed acceleration originates from a modification of the equations of the general theory of relativity; e.g. in the Dvali-Gabadadze-Porrati (DGP) braneworld theory $f(z) \approx \Omega_M(z)^{0.68}$ (Dvali et al. 2000). In general, the dependence is define by a power law $f(z) \approx \Omega_M^\gamma$ where γ is the growth index. The growth rate is therefore an important cosmological probe as is it very sensitive to modifications of gravity.

3.2 Correlation function and Power Spectrum

The large-scale structure of the Universe has proved to be very powerful for testing the cosmological model through the use of various observables such as the two-point correlation function (2PCF) $\xi(\mathbf{r})$ of the galaxy distribution and its features. The 2PCF measure the excess of probability dP , with respect to a Poissonian distribution, to find a galaxy in a given volume dV_1 at a given comoving separation vr from an other galaxy in a given volume dV_2 .

$$dP(\mathbf{r}) = \bar{n}^2(1 + \xi(\mathbf{r}))dV_1dV_2 \quad (16)$$

Where \bar{n} is the mean density. If there is no clustering (e.g. random distribution), $\xi(r) = 0$ and the probability of having a pair of galaxies is just given by the mean density squared, independently of distance. We can rewrite the 2PCF over the density contrast δ :

$$\xi(\mathbf{r}) = \langle \delta(\mathbf{r}_1)\delta(\mathbf{r}_1 + \mathbf{r}) \rangle \quad (17)$$

Where \mathbf{r}_1 is the position of a galaxy, \mathbf{r} the separation vector from an other galaxy at a position $\mathbf{r}_1 + \mathbf{r}$. The assumption that the density field is statistically homogeneous and isotropic means that the correlation function $\xi(\mathbf{r})$ is a function only of the scalar separation $r \equiv |\mathbf{r}_1 - \mathbf{r}_2|$. Thus, the inhomogeneities only depend on the value of a given scale and not on its direction. We want to trace the matter density field of the universe and look at the inhomogeneities. The density $\rho(\mathbf{r})$ may be regarded as the density of mass, or of galaxies, or of some particular objects one is interested in. We define the density contrast at position \mathbf{r} :

$$\delta = \frac{\rho(\mathbf{r}) - \bar{\rho}}{\bar{\rho}} \quad (18)$$

Where $\bar{\rho}$ is a constant in space and denote the mean density. The 2PCF of the density contrast $\delta(\mathbf{r})$ is usually written in terms of its Fourier components,

$$\delta(\mathbf{r}) = \int d^3k \delta(\mathbf{k}) e^{-i\mathbf{k} \cdot \mathbf{r}} \quad (19)$$

We can compute the correlators in Fourier space :

$$\langle \delta(\mathbf{k}_1)\delta(\mathbf{k}_2) \rangle = \int d^3\mathbf{r}_1 d^3\mathbf{r}_2 \xi(r) e^{i(\mathbf{k}_1 \cdot \mathbf{r}_1 + \mathbf{k}_2 \cdot \mathbf{r}_2)} \quad (20)$$

$$\langle \delta(\mathbf{k}_1)\delta(\mathbf{k}_2) \rangle = (2\pi)^3 \delta_D(\mathbf{k}_1 + \mathbf{k}_2) \int d^3r \xi(r) e^{i\mathbf{k} \cdot \mathbf{r}} \quad (21)$$

Where δ_D is the delta Dirac function[†] we define the power spectrum $P(k)$:

$$P(k) = \int d^3r \xi(r) e^{i\mathbf{k} \cdot \mathbf{r}}, \quad \xi(r) = \frac{1}{(2\pi)^3} \int d^3k P(k) e^{-i\mathbf{k} \cdot \mathbf{r}} \quad (22)$$

Using plane wave expansion we can rewrite Eq. 22 in spherical coordinate :

$$P(k) = \int_0^\infty dr \xi(r) 4\pi r^2 j_0(kr), \quad \xi(r) = \frac{1}{2\pi^2} \int dk k^2 j_0(kr) P(k), \quad (23)$$

Where j_0 is the spherical Bessel function of order 0. Inhomogeneities can be characterised by their statistics, e.g. their power spectrum $P(k)$. They are observed to be almost Gaussian in the

[†]By definition the Dirac function at dimension n is $\delta_D(x - x') = \frac{1}{(2\pi)^n} \int d^n r e^{-i\mathbf{r} \cdot (\mathbf{x} - \mathbf{x'})}$

CMB. The power spectrum provides a function which encodes the clustering information for the density field at all scales. The statistical properties of such a field are completely determined by its correlation functions (Peebles 1980). The first two irreducible moments are the mean and the 2-point correlation function. If fluctuations generated in the early Universe were the result of a superposition of many independent random processes, as quantum fluctuations during the inflation phase, then the Central Limit Theorem guarantees that the fluctuations will form a multivariate Gaussian[‡]. In this case, the mean and 2-point correlation function completely specify the statistical properties of the field and, by definition all higher correlation functions vanish.

It is useful to make a connection to other quantities commonly used to probe growth. First of all, we define a commonly used quantity in cosmology, the root mean square amplitude of mass fluctuations σ_R , which is given by the integral over the power spectrum :

$$\sigma^2(R) = \int_0^\infty dk \frac{k^2}{2\pi^2} P(k) W^2(kR) \quad (24)$$

where $W(x) = 3j_1(x)/x$ is a window function. $\sigma_R(z)$ encodes the amount of matter fluctuations averaged over a sphere of radius R at redshift z , assuming that the fluctuations are fully linear. In cosmology we usually describe the normalization of the fluctuations in the Universe today at $\sigma_8(z=0)$ for a sphere of radius 8Mpc. We can rewrite the power-spectrum time dependence as:

$$P(k, 0) = \frac{\sigma_8^2(z=0)}{\sigma_8^2(z)} P(k, z) \quad (25)$$

Today the value of $\sigma_8 \approx 0.82$ (Planck Collaboration et al. 2014).

[‡]The Central Limit Theorem states that, in some situations, a sum of random independent variables approaches a normal distribution as the number of variables gets larger

4 Redshift-space distortions as probe of structure growth

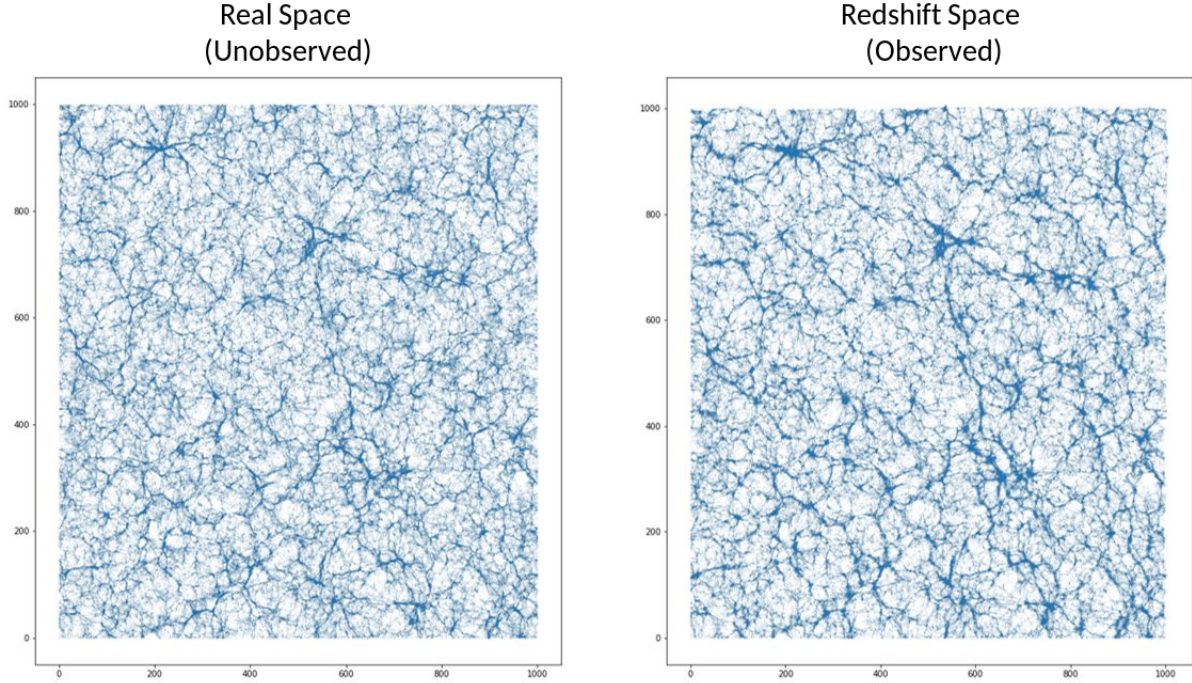


Figure 3: An example of a slice through a more than 300 billion particles dark matter particles Λ CDM simulations at redshift $z = 0$ ($\Omega_m = 0.3089$, $\Omega_\Lambda = 0.6911$, $\sigma_8 = 0.8174$, $h = H_0/100 = 0.6774$). The box size is $1 h^{-1}\text{Mpc}$, the slice thickness $10 h^{-1}\text{Mpc}$. *Left panel* is the clustering in real space and *right panel* in redshift space (including velocities). Each dot represents a halo. Note the clear amplification of clustering in redshift space.

4.1 Redshift-space distortions

In redshift survey we use redshift to estimate galaxy distances rather than true distance. However, galaxies have peculiar velocities \mathbf{v} relative to the general Hubble expansion causing a Doppler shift in addition to the redshift. In redshift-space, peculiar velocities displace galaxies on the direction of the los , hence only the parallel velocity component to the los \mathbf{v}_\parallel will modify the true distance of the galaxies (Fig.4). That introduce anisotropy in the pattern of galaxy clustering. This effect is what we called in observational cosmology Redshift-Space Distortions (RSD). It is necessary to distinguish between the galaxy's redshift distance $\mathbf{s} \equiv c \cdot \hat{\mathbf{z}}$ and its true distance $\mathbf{r} = H_0 \times D$. The redshift distance \mathbf{s} of a galaxy differs from the true distance \mathbf{r} by its peculiar velocity $v_l(\mathbf{x}) = \mathbf{v} \cdot \hat{\mathbf{l}}$ along the line of sight (los) $\hat{\mathbf{l}}$:

$$\mathbf{s} = \mathbf{r} + \frac{v_l(\mathbf{x})}{aH(a)} \cdot \hat{\mathbf{l}} \quad (26)$$

Considering a plane-parallel approximation, when the observer is far enough from the galaxies pair to consider that los of both galaxies are parallel, we can fully describe the configuration of the galaxy pair with only 2 distances : s_\parallel and s_\perp , the parallel and perpendicular component to the los (see Figure 4). Note that as we see before only the parallel component of the velocity is impacted by peculiar velocities therefore, the perpendicular component is the same in redshift-space than in

real space $s_{\perp} = r_{\perp}$. The equivalence between the coordinate \mathbf{s} , μ and s_{\parallel} , s_{\perp} is trivial:

$$\mathbf{s}^2 = s_{\parallel}^2 + s_{\perp}^2 \quad (27)$$

$$\mu = \frac{r_{\perp}}{s} \quad (28)$$

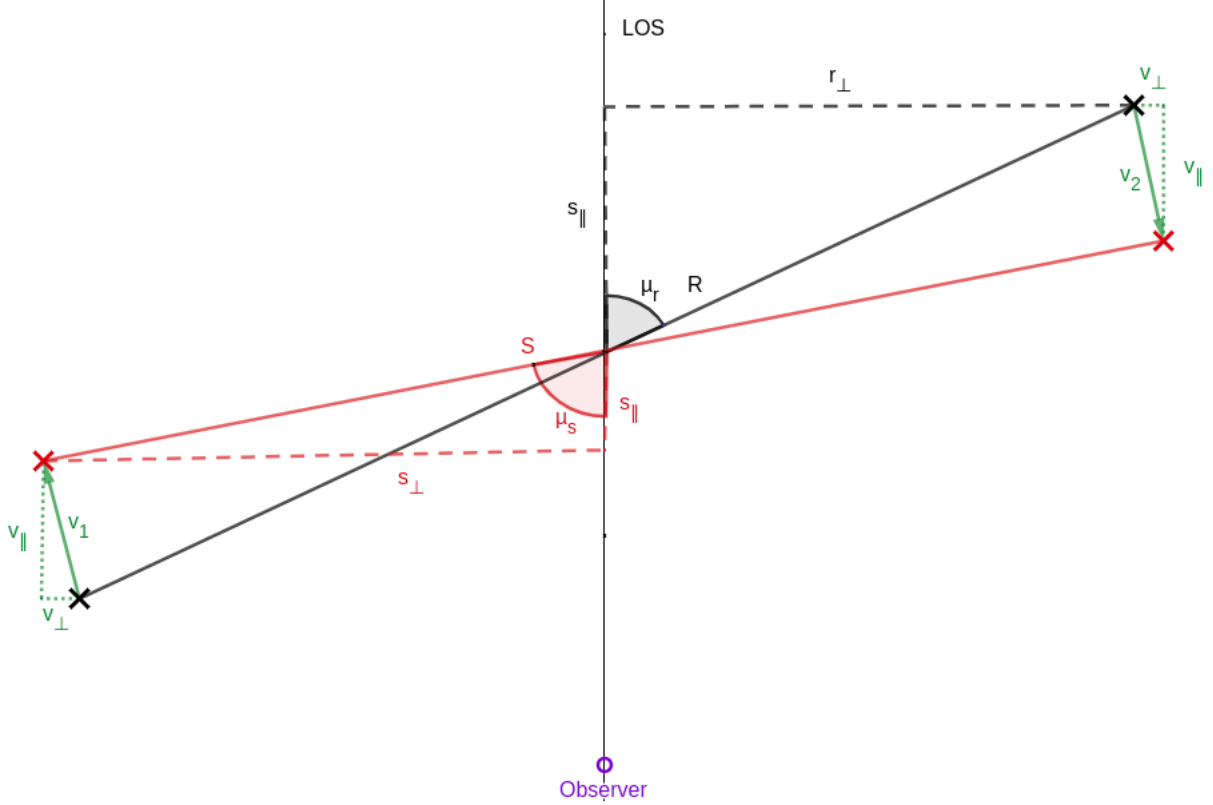


Figure 4: Real space to redshift space mapping for a pair of galaxies due to peculiar velocities (green). Red components are corresponding to redshift space and black component to real space. The position of the object is shifted along the line of sight due to peculiar velocities. The observer is from the bottom.

Similarly to §3.2, we can write the redshift correlation function $\xi_s(s_{\parallel}, s_{\perp})$ for a galaxy pair in redshift-space:

$$\xi^s(s, \mu_s) = \frac{1}{(2\pi)^3} \int d^3\mathbf{k} P^s(k, \mu_k) e^{-ik s \mu_s} \quad (29)$$

Where \mathbf{s} is the distance between the galaxy pair and $\mu_s = \hat{\mathbf{s}} \cdot \hat{\mathbf{l}}$ the cosine of the angle between \mathbf{s} and the line of sight los . Physically, the redshift correlation function $\xi_s(s_{\parallel}, s_{\perp})$ is the mean fractional excess of galaxy neighbours of a galaxy at separations s_{\parallel} and s_{\perp} to the line of sight. A representation of the redshift-space correlation function is shown in the left panel of Figure 5. Peculiar velocities are important because they are related to the density perturbation δ via the continuity equation (Eq.15). Since peculiar velocities are driven by gravity, they are a direct consequence of the growth of structure and could predict deviations from GR by measuring smaller or larger anisotropic distortions in the observed redshift-space clustering (Guzzo et al. 2008). In fact, slower or faster growth give smaller or larger anisotropic distortions in the observed redshift-space clustering. There are two main signatures of peculiar velocities on the shape of redshift-space clustering. Figure 5

shows how peculiar velocities produce these patterns. At large scales ($> 5 h^{-1}\text{Mpc}$), galaxies that fall into clusters look squashed along the line of sight in redshift space. This squashing effect leads to an increase of the clustering amplitude along the line of sight and its call Kaiser effect. Figure 3 shows the clustering amplification along filaments of the cosmic-web. At small scales ($< 5 h^{-1}\text{Mpc}$) the internal velocity dispersion becomes larger and galaxies appear inside out in the overdense region, elongating clusters along the line of sight, leading to the so-called “finger of god” effect. The large scale squashing effect can be detected statistically, from the distortion of the redshift space correlation function ξ_s (Hamilton 1998).

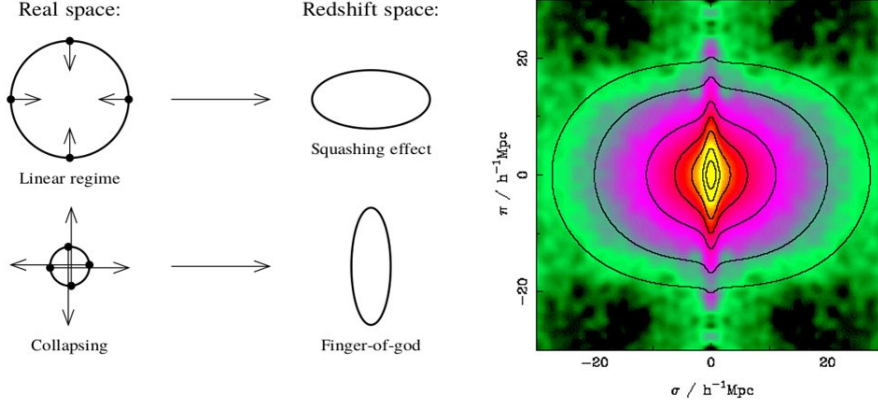


Figure 5: The *right panel* from Hamilton (1998) represent how peculiar velocities modify the pattern of redshift-space clustering and lead to redshift distortion. The dots are ‘galaxies’ undergoing infall towards a spherical overdensity. The arrows represent their peculiar velocities. At large scales (top), the peculiar infall velocities are small compared to the radius of the spherical overdensity, and appears squashed. At smaller scales (bottom), galaxies are collapsing in the overdense region, their peculiar infall velocities are larger and they appear inside out in redshift space, leading to the fingers-of-god. *Left panel* shows the galaxy-galaxy 2-PCF measured from redshift survey 2dFGRS (Peacock et al. 2001). σ and π represent respectively the perpendicular component r_{\perp} and the parallel component s_{\parallel} to the los

4.2 Kaiser model of linear Redshift Space Distortion

The first theoretical approach of linear RSD was made by Kaiser (1987). The starting point is to assume the mass conservation between real and redshift space :

$$\rho_s(\mathbf{s})d^3\mathbf{s} = \rho(\mathbf{r})d^3\mathbf{r} \quad (30)$$

That means the number of galaxy is the same in redshift and real space. We can rewrite previous equation in terms of overdensities :

$$1 + \delta_s(\mathbf{s}) = [1 + \delta_r] \left| \frac{d^3\mathbf{s}}{d^3\mathbf{r}} \right|^{-1} \quad (31)$$

In the plan parallel approximation the Jacobian of the real- to redshift-space transformation can be simply written as :

$$\left| \frac{d^3\mathbf{s}}{d^3\mathbf{r}} \right|^{-1} = 1 - f\partial_{\parallel}u_l \quad (32)$$

Where $u_l = v_l(\mathbf{r})/(faH(a))$ and f the linear growth rate. Substituting Eq.(31) and (32) we get :

$$1 + \delta^s(\mathbf{s}) = [1 + \delta^r](1 - f\partial_{\parallel}u_l)^{-1} \quad (33)$$

To derive the solution in linear regime we consider small perturbations $\delta \ll 1$, small velocity variations $f\partial_{\parallel}u_l \ll 1$, we assume that velocities are small according to the scale r , $fu_l/r \ll 1$ and scale of perturbations are smaller than the distance from us. Under these hypothesis Kaiser derive then the mapping real to redshift coordinates in mass density contrast :

$$\delta^s(\mathbf{k}) = (1 + f\mu_k^2)\delta(k) \quad (34)$$

with $\mu_k = k_l/k$ the cosine of the angle between the wave vector \mathbf{k} and the *los*. We can write the previous equation in terms of Power spectrum using equations in §3.2 :

$$P^s(k, \mu_k) = (1 + f\mu^2)^2 P^r(k) \quad (35)$$

And substituting Eq.(35) and (29), we obtain:

$$\xi^s(s, \mu_s) = \frac{(1 + f\mu^2)}{(2\pi)^3} \int d^3\mathbf{k} P^r(k) e^{-ik_s\mu_{ks}} \quad (36)$$

This equation makes the mapping to redshift coordinates, including the anisotropic feature of RDS at large scale and the bias parameter due to the change between real mass density field and observed density field through galaxies or clusters. All the information of the corresponding correlation function is enclosed in the coefficients of the first three even Legendre polynomials \mathcal{L}_0 , \mathcal{L}_2 and \mathcal{L}_4 :

$$\xi^s(s, \mu_s) = \sum_l \xi_l^s(s) \mathcal{L}_l(\mu_s) \quad (37)$$

The multipole are given by Hamilton (1998):

$$\xi_l^s(s) = \frac{2l+1}{2} \int_{-1}^1 d\mu \xi^s(s, \mu) \mathcal{L}_l(\mu) \quad (38)$$

Since they must be anisotropic odd moments and no power higher than μ^4 vanish (Scoccimarro 2004). Finally, we can write the 3 non-zeros multipole from Hamilton (1998) :

$$\xi_0^s(s) = \left(1 + \frac{2}{3}f + \frac{1}{5}f^2\right) \frac{1}{2\pi^2} \int_0^\infty dk k^2 P_m^r(k) j_0(ks) \quad (39)$$

$$\xi_2^s(s) = -\left(\frac{4}{3}f + \frac{4}{7}f^2\right) \frac{1}{2\pi^2} \int_0^\infty dk k^2 P_m^r(k) j_2(ks) \quad (40)$$

$$\xi_4^s(s) = \left(\frac{8}{35}f^2\right) \frac{1}{2\pi^2} \int_0^\infty dk k^2 P_m^r(k) j_4(ks) \quad (41)$$

4.3 Galaxy bias

We have just seen the importance to study the evolution of LSS over cosmic time to study the expansion history and test the theory of gravity. To study the LSS we use statistical tools such as the 2PCF. We use object, such as galaxies or clusters to compute the 2PCF. LSS is composed of the entire matter in the universe. But, what we can see from LSS is the baryonic matter (e.g. galaxies, clusters, superclusters) that represent only 16% of the entire matter in the universe. The remaining part of the matter is the dark matter that we can not see. However, baryonic matter follow the rules of gravity, and will be used as a tracer of dark matter in the universe and consequently of the density field in the universe. It is the only way to "see" the LSS. The major problem of following galaxies as a tracer of density is that it do not represent the underlying DM density field but it may be a biased realization of it. In the literature, the simplest model of bias postulates that galaxies and matter density fields are related one to another by a constant factor, the linear bias factor b :

$$\delta_g(\mathbf{x}) = b\delta_M(\mathbf{x}) \quad (42)$$

The bias parameter include additional non-cosmological parameters to describe the relation between galaxies and DM.

$$b = \frac{\sigma_g}{\sigma_m}$$

Where σ represent the standard deviation of δ on linear scales. Similarly, it implies that the power spectra obey in the same way $P_g(k) = bP_M(k)$. We can rewrite the derivation of Kaiser linear model in §4.2 using biased tracer (e.g. galaxies) instead of the true matter density field δ_M^s . We introduce the the galaxy distortion parameter $\beta = f/b$ and we obtain :

$$P_g^s(k, \mu) = b^2(1 + \beta\mu^2)^2 P^r(k) \quad (43)$$

All the odd moments and no power higher than μ^4 vanish. Therefore we can write the 3 non-zeros multipoles from Hamilton (1998) :

$$\xi_0^s(s) = b^2 \left(1 + \frac{2}{3}\beta + \frac{1}{5}\beta^2\right) \frac{1}{2\pi^2} \int_0^\infty dk \, k^2 P_m^r(k) j_0(ks) \quad (44)$$

$$\xi_2^s(s) = -b^2 \left(\frac{4}{3}\beta + \frac{4}{7}\beta^2\right) \frac{1}{2\pi^2} \int_0^\infty dk \, k^2 P_m^r(k) j_2(ks) \quad (45)$$

$$\xi_4^s(s) = b^2 \left(\frac{8}{35}\beta^2\right) \frac{1}{2\pi^2} \int_0^\infty dk \, k^2 P_m^r(k) j_4(ks) \quad (46)$$

The Kaiser formula Eq.(43) shows the degeneracy between the growth rate f and the root mean square amplitude of mass fluctuations σ_8 (Eq.(25)). This degeneracy complicates the extraction of the growth function from the isotropic power spectrum derived from clustering of cosmic sources. Thus, we can measure the growth rate f assuming a fiducial value of σ_8 or we can measure the product $f\sigma_8$. Figure 4 6, display the measurement of $f\sigma_8$ done by previous galaxy redshift surveys. Most of the measurement are consistent with the General Relativity $f = \Omega^{0.55}$ (thick solid dashed curve).

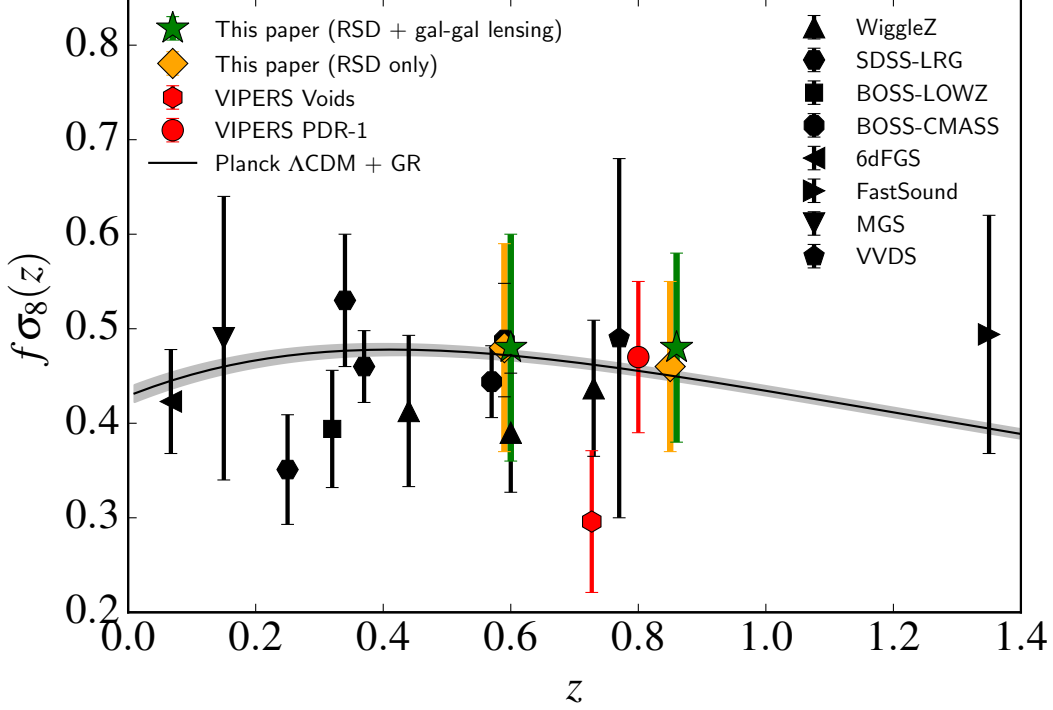


Figure 6: This plot from de la Torre et al. (2017) shows the evolution of $f\sigma_8$ as a function of redshift. The results are from VVDS (Guzzo et al. 2008), SDSS LRG (Ω; Samushia et al. (2012)), WigglyZ (Blake et al. 2012), BOSS (Reid et al. 2012), 6dFGS (Beutler et al. 2012), VIPERS (de la Torre et al. 2013), MGS (Howlett et al. 2015), FastSound (Okumura et al. 2016), BOSS-LOWZ Gil-Marín et al. (2016), BOSS-CMASS (Chuang et al. 2016), and VIPERS PDR-2 voids (Hawken et al. 2017) are shown with the different symbols. The solid curve and associated shaded area correspond to the expectations and 68 uncertainty for General Relativity in a Λ CDM background model set to TT+lowP+lensing Planck 2015 predictions (Planck Collaboration et al. 2016)

5 Gaussian streaming model

As we see in §4.1, galaxy peculiar velocities induce deformation in the pattern of galaxy clustering. The two main effects are the squashing effect ("Kaiser effect") along the LOS at large scale and the elongation of non-linear structures ("Fingers of God") at small scales. The squashing effect at large scale is well described by the linear theory (§4.2). However, on small scales, Kaiser model does not work anymore. The streaming model has been introduced to map real-space correlation function $\xi_r(r)$ on to redshift-space correlation function $\xi_s(s)$ (Peebles (1980); Fisher (1995); Scoccimarro (2004)) including both linear and non-linear scales. In this model distortions in redshift-space are given by a convolution of the real-space correlation function with the pairwise velocity probability distribution function (PDF) along the line of sight :

$$1 + \xi_m^s(s_{\parallel}, s_{\perp}) = \int dy [1 + \xi_m^r(r)] * \mathcal{P}(v_{12} = s_{\parallel} - r_{\perp}, \mathbf{r}) \quad (47)$$

Where $r^2 = r_{\parallel}^2 + r_{\perp}^2$ is the separated distance between 2 galaxies, s_{\perp} is the transverse separation (real and redshift-space), s_{\parallel} is the parallel separation along the LOS in redshift space and v_{12} the mean relative peculiar velocity of two galaxies separated by \mathbf{r} . The pairwise velocity PDF $\mathcal{P}(v_l, \mathbf{r})$ is the probability that a pair with real space separation \mathbf{r} has relative LOS velocity v_l . The physical inter-

pretation of Eq. 47 is clear: \mathcal{P} maps the pairs at separation \mathbf{r} to separation \mathbf{s} due to relative velocity with probability $P(r_\perp - s_\perp, \mathbf{r})$. \mathcal{P} is scale-dependent, that means correlations in redshift-space are created by taking random pairs in real space and mapping them to redshift space differently at different scales. The form of $\mathcal{P}(v_l, \mathbf{r})$ is arbitrary, then, the first approximation made by Fisher (1995), Gorski (1988) to re-covert linear theory predictions is to assume that both density and velocity fields are gaussian and related to one another. In this case, the joint distribution of densities and velocities is a multi-variate Gaussian. From linear theory, we can derive density/velocity coupling $\langle \delta v \rangle$, velocity/velocity coupling $\langle \mathbf{v}_1 \mathbf{v}_2 \rangle$ and the root mean square (rms) velocity σ_v . Reid & White (2011) reproduce the relevant linear theory velocity prediction generalised to linearly biased tracers with bias b (Fisher 1995):

$$\mathbf{v}_{12}(\mathbf{r}) = -\hat{r} \frac{fb}{\pi^2} \int_0^\infty dk k P_m^r(k) j_1(kr) \quad (48)$$

$$\Psi_\parallel(\mathbf{r}) = \frac{f^2}{2\pi^2} \int_0^\infty dk P_m^r(k) \left[j_0(kr) - \frac{2j_1(kr)}{kr} \right] \quad (49)$$

$$\Psi_\perp(\mathbf{r}) = \frac{f^2}{2\pi^2} \int_0^\infty dk P_m^r(k) \frac{j_1(kr)}{kr} \quad (50)$$

$$\sigma_{12}^2(\mathbf{r}, \mu_r^2) = 2 \left[\sigma_v^2 - \mu_r^2 \Psi_\parallel(r) - (1 - \mu_r^2) \Psi_\perp(r) \right] \quad (51)$$

$$\sigma_v^2 = \frac{1}{3} \frac{f^2 b^2}{2\pi^2} \int_0^\infty dk P_m^r(k) \quad (52)$$

Where j_l is the spherical Bessel function of order l , $\mu_r = \hat{l} \cdot \hat{r}$ denotes the angle between the LOS and the pair separation vector \mathbf{r} , σ_v is the one dimensional rms velocity and σ_{12} the velocity dispersion along the LOS. Scoccimarro (2004) derives the exact result Eq. 53 for the redshift space correlation function in the case where both density and velocity fields are Gaussian and related to one another as in linear theory.

$$1 + \xi_g^s(r_\sigma, r_\pi) = \int \frac{dy}{\sqrt{2\pi\sigma_{12}^2(y)}} \exp \left[-\frac{(r_\pi - y)^2}{2\sigma_{12}^2(y)} \right] \times \left[1 + \xi_g^r(r) + \frac{y}{r} \frac{(r_\pi - y)v_{12}(r)}{\sigma_{12}^2(y)} - \frac{1}{4} \frac{y^2}{r^2} \frac{v_{12}^2(r)}{\sigma_{12}^2(y)} \left(1 - \frac{(r_\pi - y)^2}{\sigma_{12}^2(y)} \right) \right] \quad (53)$$

Even for the exact result in the Gaussian case, the corresponding pairwise velocity PDF is non-Gaussian; however, near its peak it can be approximated by a Gaussian centred on the parallel component of the pairwise velocity $\mu_r \mathbf{v}_{12}(r)$ (Scoccimarro (2004)). Thus, in the Gaussian Streaming Model (GSM), pairwise velocity PDF is given by :

$$\mathcal{P}(v_{12} = s_\parallel - r_\perp, \mathbf{r}) = \frac{1}{\sqrt{2\pi\sigma_{12}^2(\mathbf{r}, \mu_r)}} \exp \left[-\frac{s_\parallel - r_\parallel - \mu_r v_{12}(\mathbf{r})}{2\sigma_{12}^2(\mathbf{r}, \mu_r)} \right] \quad (54)$$

In linear dynamics, Gaussianity implies that only the two first moment of the pairwise velocity PDF do not vanish : $\mu_r \mathbf{v}_{12}(\mathbf{r})$ and $\sigma_{12}(\mu_r, \mathbf{r})$. Linear theory can evaluate the moment of pairwise velocity PDF but it never gives a good approximation to the second moment. Therefore, we have to investigate other non-linear approach to better constrain these two moments. Different approaches have been develop to generated the first two moments of the pairwise PDF, on the one hand the improvement of Kaiser theory by using Eulerian Perturbation Theory (Taruya et al. 2010), on the other hand Matsubara (2008) developed a Lagrangian perturbation theory (LPT) to describes redshift-space distortion. In the next section we go further with the LPT and shows the detail calculation to generate the pairwise velocities moments.

6 Convolution Lagrangian Perturbation Theory

A different way to approach non linear regime of RSD is to go through Lagrangian coordinate. (Matsubara 2008) laid out the formalism for including redshift-space distortions and non-linear local Lagrangian biasing within Lagrangian perturbation theory. Here we provide a review of LPT from Matsubara and derive the prediction of pairwise velocities moments for the Convolution Lagrangian Perturbation Theory (CLPT) model (Carlson et al. 2013).

6.1 Lagrangian Perturbation Theory

In the Lagrangian approach to cosmological fluid dynamics, we trace the trajectory of an individual fluid element through space and time. Consider a fluid element located at position \mathbf{q} at some initial time t_0 , its position at time t can be written in terms of the Lagrangian displacement field Ψ :

$$\mathbf{x}(\mathbf{q}, t) = \mathbf{q} + \Psi(\mathbf{q}, t) \quad (55)$$

Where $\Psi(\mathbf{q}, t_0) = 0$. Every elements of the cosmological fluid is describe by its own Lagrangian coordinate \mathbf{q} . At a give time t we can do the mapping $\mathbf{q} \leftrightarrow \mathbf{x}$ as a change of variable.

The displacement fields Ψ is a fundamental variable of the mass density field that describe fully the motion of the cosmological fluid. In the LPT, the displacement field is expand in a perturbative series :

$$\Psi(\mathbf{q}, t) = \Psi^{(1)}(\mathbf{q}, t) + \Psi^{(2)}(\mathbf{q}, t) + \Psi^{(3)}(\mathbf{q}, t) + \dots \quad (56)$$

The solution at first order is the Zel'Dovich approximation (Zel'Dovich 1970). Considering mass continuity between the Eulerian density field, and corresponding Lagrangian density field we get (in terms of density contrast $\delta = \rho/\bar{\rho} - 1$):

$$[1 + \delta_m(\mathbf{x}, t)]d^3x = [1 + \delta_m(\mathbf{q}, t_0)]d^3q \quad (57)$$

If the initial time t_0 is taken to be early enough, the initial matter fluctuations $\delta_m(\mathbf{q}, t)$ are arbitrarily small, so that we may formally express the Eulerian density field in terms of the Lagrangian displacement field as:

$$1 + \delta_m(\mathbf{x}, t) = [1 + \delta_m(\mathbf{q}, t_0)] \left| \frac{d^3\mathbf{x}}{d^3\mathbf{q}} \right|^{-1} \quad (58)$$

$$1 + \delta(\mathbf{x}, t) = \int d^3q \delta_D^3[\mathbf{x} - \mathbf{q} - \Psi(\mathbf{q}, t)]$$

Where δ_D^3 is 3-dimensional Dirac's delta function.

6.2 Biased Tracer in LPT

However, we observed object as haloes or galaxies to trace the matter density field. These object in the cosmic fluid are biased and then, not uniformly distributed in Lagrangian space. In his paper Matsubara (2008) assume locality of the bias in Lagrangian space. Its means that initial locations q_i of object came from a distribution that is a locally biased function of the smoothed matter density field :

$$\rho_{obj}^L = \bar{\rho}_{obj} F(\delta_R(\mathbf{q})) \quad (59)$$

Where $\bar{\rho}_{obj}$ is the comoving mean density of the biased objects, which is common in Lagrangian space and in Eulerian space. The function $F(\delta)$ is called the Lagrangian bias function which describe

the bias dependence of the object. The correspondence between local lagrangian bias and eulerian bias value is given by $b^E = 1 + b^L$ (Matsubara 2008). We can rewrite Eq. 58 for bias tracer:

$$1 + \delta(\mathbf{x}, t) = \int d^3q F(\delta_R(\mathbf{q})) \delta_D^3[\mathbf{x} - \mathbf{q} - \Psi(\mathbf{q}, t)] \quad (60)$$

We can evaluate the power spectrum of biased objects in Eulerian space by taking the Fourier transform of Eq. 60 ($F(\delta) \xrightarrow{\text{FT}} \tilde{F}(\lambda)$):

$$1 + \delta(\mathbf{x}, t) = \int d^3q \int \frac{d^3k}{(2\pi)^3} \int \frac{d\lambda}{2\pi} \tilde{F}(\lambda) e^{i[\lambda\delta_R(\mathbf{q}) + \mathbf{k} \cdot (\mathbf{x} - \mathbf{q} - \Psi(\mathbf{q}))]} \quad (61)$$

Then, we can derive the 2-point correlation function for the biased tracer X :

$$1 + \xi_X(\mathbf{r}) = \int d^3q \int \frac{d^3k}{(2\pi)^3} e^{i\mathbf{k} \cdot (\mathbf{q} - \mathbf{r})} \int \frac{d\lambda_1}{2\pi} \frac{d\lambda_2}{2\pi} \tilde{F}_1 \tilde{F}_2 K(\mathbf{q}, \mathbf{k}, \lambda_1, \lambda_2), \quad (62)$$

Where we define $K(\mathbf{q}, \mathbf{k}, \lambda_1, \lambda_2)$:

$$K(\mathbf{q}, \mathbf{k}, \lambda_1, \lambda_2) = \left\langle e^{i(\lambda_1\delta_1 + \lambda_2\delta_2 + \mathbf{k} \cdot \vec{\Delta})} \right\rangle \quad \text{and} \quad \Delta \equiv \vec{\Psi}_2 - \vec{\Psi}_1 \quad (63)$$

6.3 Redshift space

As we see in §4.1 the position of an object located at true comoving position \mathbf{x} , will be different from its observed position due to peculiar velocity (Eq.26). In the Lagrangian approach, including redshift-space distortions requires only a simple additive offset of the displacement field. The peculiar velocity of a fluid element, labeled by its Lagrangian coordinate \mathbf{q} , is at any time given by $\mathbf{v}(\mathbf{q}) = a\dot{\mathbf{x}}(\mathbf{q}) = a\dot{\Psi}(\mathbf{q})$. So, the apparent displacement field in redshift space of a fluid element is:

$$\Psi^{(s)} = \Psi + \frac{\hat{l} \cdot \dot{\Psi}}{H} \hat{l} \quad (64)$$

The relation between displacement fields in Eq. 64 is exactly linear even in the nonlinear regime. The time dependence of the n^{th} perturbative term in Eq. 56 is approximately given by $\Psi^{(n)} D^n$ where $D(t)$ is the linear growth rate. We derive this equation to obtain $\dot{\Psi}^{(n)} = nHf\Psi^{(n)}$ where f is the growth factor. The mapping to redshift-space may then be achieved, order-by-order, via the matrix $R_{ij}^{(n)} = \delta_{ij} + nf\hat{l}_i\hat{l}_j$ as $\Psi^{s(n)} = R^{(n)}\Psi^{(n)}$ (Bernardeau et al. 2002).

6.4 CLPT predictions

We present the result of the correlation function $\xi(\mathbf{r})$, and the pairwise velocity moments $v_{12}(\mathbf{r})$ and $\sigma_{12}(r)$ from the derivation in Lagrangian Perturbation Theory made by Carlson et al. (2013) and Wang et al. (2014). Details of the entire derivation was done by Carlson et al. (2013) and Wang et al. (2014), here we only recall the principle result. We define the velocity generating function $Z(\mathbf{r}, \mathbf{J})$ by (Eq.14 of Wang et al. (2014)), when we take successive derivative we get the moments the a distribution function Z :

$$Z(\mathbf{r}, \mathbf{J}) = \int d^3q \int \frac{d^3k}{(2\pi)^3} i\mathbf{k} \cdot (\mathbf{q} - \mathbf{r}) \int \frac{d\lambda_1}{2\pi} \frac{d\lambda_2}{2\pi} \times \tilde{F}(\lambda_1) \tilde{F}(\lambda_2) \left\langle \exp i \left(\lambda_1\delta_1 + \lambda_2\delta_2 + \mathbf{k} \cdot \vec{\Delta} + \mathbf{J} \cdot \dot{\vec{\Delta}}/H \right) \right\rangle \quad (65)$$

Where $Z(\mathbf{r}, 0) = 1 + \xi(r)$, the first derivative $Z(\mathbf{r}, 1) = v_{12}(\mathbf{r})$ and the second derivative $Z(\mathbf{r}, 2) = \sigma_{12}(\mathbf{r})$. He generalizes the definitions of the functions K , L , and M in Carlson et al. (2013) to include \mathbf{J} :

$$\begin{aligned}
X &= \lambda_1 \delta_1 + \lambda_2 \delta_2 + \mathbf{k} \cdot \vec{\Delta} + \mathbf{J} \cdot \vec{\Delta}/H , \\
K_{p, \{i_1 \dots i_p\}}(\mathbf{q}, \mathbf{k}, \lambda_1, \lambda_2) &= \left\langle \left(-i \frac{\partial}{\partial \mathbf{J}_{i_k}} \right)^p iX \right\rangle \Big|_{\mathbf{J}=0} , \\
L_{p, \{i_1 \dots i_p\}}(\mathbf{q}, \mathbf{k}) &= \int \frac{d\lambda_1}{2\pi} \frac{d\lambda_2}{2\pi} K_{p, \{i_1 \dots i_p\}}(\mathbf{q}, \mathbf{k}, \lambda_1, \lambda_2) , \\
M_{p, \{i_1 \dots i_p\}}(\mathbf{r}, \mathbf{q}) &= \int \frac{d^3 k}{(2\pi)^3} i\mathbf{k} \cdot (\mathbf{q} - \mathbf{r}) L_{p, \{i_1 \dots i_p\}}(\mathbf{q}, \mathbf{k}) , \\
&\left\langle [1 + \delta(\mathbf{x})][1 + \delta(\mathbf{x} + \mathbf{r})] \left\{ \prod_{k=1}^p [v_{i_k}(\mathbf{x} + \mathbf{r}) - v_{i_k}(\mathbf{x})] \right\} \right\rangle \\
&= \int d^3 q M_{p, \{i_1, \dots, i_p\}}(\mathbf{r}, \mathbf{q}) .
\end{aligned} \tag{66}$$

The first subscript of these functions indicates the number of derivative terms p , and the second is a list containing the Cartesian indices of the p derivatives. Therefore, from Eq.(65) and (66) we get :

$$\begin{aligned}
1 + \xi(\mathbf{r}) &= \int d^3 q M_0(\mathbf{r}, \mathbf{q}) \\
v_{12,n}(\mathbf{r}) &= [1 + \xi(r)]^{-1} \int d^3 q M_{1,n}(\mathbf{r}, \mathbf{q}) \\
\sigma_{12,nm}^2(\mathbf{r}) &= [1 + \xi(r)]^{-1} \int d^3 q M_{2,nm}(\mathbf{r}, \mathbf{q})
\end{aligned} \tag{67}$$

The pairwise velocity $v_{12,n}$ is projected along the direction of pair separation vector, e.g. $v_{12} = v_{12,n} \hat{r}_n$. In order to obtain the velocity dispersion components parallel σ_{\parallel} and perpendicular σ_{\perp} to the pairwise separation unit vector \hat{r} , we project $\sigma_{12,nm}^2$ into different directions:

$$\sigma_{\parallel}^2 = \sigma_{12,nm}^2 \hat{r}_n \hat{r}_m , \quad \sigma_{\perp}^2 = (\sigma_{12,nm}^2 \delta_{nm}^K - \sigma_{\parallel}^2)/2 . \tag{68}$$

To compute $M_{p, \{i_1 \dots i_p\}}$, Wang et al. (2014) expand $K(\mathbf{q}, \mathbf{k}, \lambda_1, \lambda_2)$ using the cumulant expansion theorem[§]. Functions $M_0(\mathbf{r}, \mathbf{q})$, $M_{1,n}(\mathbf{r}, \mathbf{q})$, $M_{2,nm}(\mathbf{r}, \mathbf{q})$ are define in appendix A.

[§]The cumulant expansion theorem expand the expectation value of $\langle e^{iX} \rangle$ in terms of cumulants, $\langle e^{iX} \rangle = \exp\left(\sum_{n=1}^{\infty} \frac{i^n}{n!} \langle X^n \rangle\right)$, where $\langle X^N \rangle$ denotes the N th cumulant of the random variable X .

7 Code/Numerical analysis

In this section we present the numerical analysis that we performed to evaluate the prediction of pairwise velocity moments in the both cases of linear theory and CLPT for the Gaussian Streaming Model. We implemented in C codes the linear and CLPT predictions[¶].

7.1 Code Process

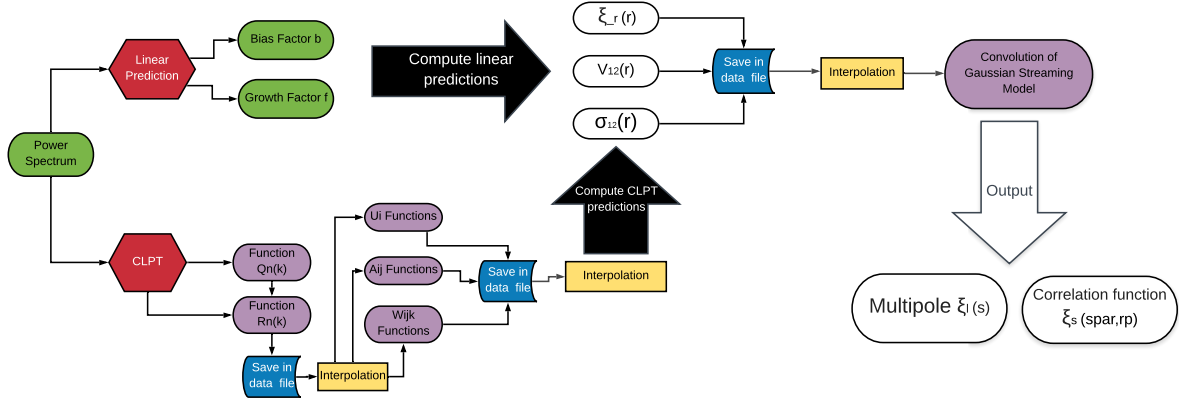


Figure 7: Schematic view of the progress of the code. Green boxes are the input, red boxes the different models, purple boxes the functions and white boxes the output. Both linear and CLPT predictions of pairwise velocity function are compute independently. Then, we take the results of each predictions to perform the convolution of the Gaussian Streaming Model Eq. 47. We finally obtain the 2-PCF in redshift space and the first 3 multipoles for both predictions.

Figure 7 present the code process. The code is divided in two main part, the first with the linear prediction of the pairwise velocity moment from Fisher (1995), and the other with the prediction from the CLPT model (Wang et al. 2014). Then, from CLPT or linear prediction we compute the convolution of GS model Eq.47 to get the correlation function $\xi_s(s_{\parallel}, s_{\perp})$ and 3 non-vanishing multipoles $\xi_0(s)$, $\xi_2(s)$, $\xi_4(s)$. For both codes the power spectrum (PS) is an input file. PS is calculated from CAMB (Lewis & Bridle 2002) and cosmological parameter are imprint in the power spectrum (Ω_M , Ω_{Λ} , h , σ_8). In order to compute the linear prediction of the streaming model, we first evaluate the integration in Eq. 49 to 52 using QUADPACK numerical integration algorithms from GSL library (Galassi 2018). QUADPACK is a library which estimates integrals for adaptive and non-adaptive integration of general functions, using numerical quadrature with specialised routines for specific cases (singularities, oscillatory integrals...) (Piessens et al. 1983). Each algorithms computes an approximation to a definite integral of the form:

$$I = \int_a^b f(x)w(x)dx \quad (69)$$

where $w(x)$ is a weight function (for general integrands $w(x) = 1$).

[¶]The code is available upon request at antoinerocher01370@gmail.com

We provides absolute and relative error bounds. Errors define the accuracy of the integral evaluation $|RESULT - I| \leq \max(\text{epsabs}, \text{epsrel}|I|)$, where *RESULT* is the numerical approximation obtained by the algorithm. The algorithms attempt to estimate the absolute error $ABSEERR = |RESULT - I|$ in such a way that the following inequality holds, $|RESULT - I| \leq ABSEERR \leq \max(\text{epsabs}, \text{epsrel}|I|)$. The algorithms for general functions (without a weight function) are based on Gauss-Kronrod rules. We use QAWO algorithm (adaptive integration for oscillatory functions) to evaluate the integral including Bessel function j_n . We evaluate those function between s_{min} and s_{max} in $h^{-1}\text{Mpc}$. We generally take $s_{min} = 1h^{-1}\text{Mpc}$ and $s_{max} = 130h^{-1}\text{Mpc}$ to get the finger of gods feature on small scales and the BAO feature on large scales. Then, we use theses results to compute the convolution equation of the streaming model Eq.47 and the multipoles Eq.38. To optimize the rapidity of the code execution we save results in text files and perform interpolation. We used cubic spline interpolation technique and the convolution is evaluate using Gauss quadrature with 128 points. Finally, we evaluate multipoles Eq.38 using a Gauss-Legendre quadrature. Then the final output are store in text file. The cubic spline interpolation is a piecewise continuous curve, passing through each of the data points. Each separation interval in the data set is evaluating by one single cubic polynomial for each interval, with its own coefficients:

$$S_i(x) = a_i(x - x_i)^3 + b_i(x - x_i)^2 + c_i(x - x_i) + d_i \quad (70)$$

Gauss quadrature is an approximation to compute an integral by using a weighted sum at specified points within the domain of integration :

$$\int_b^a F(x)dx \approx \sum_i^n \omega_i f(x_i) \quad (71)$$

where n is the number of point and ω_i the weight. In the case of Gauss-Legendre quadrature the weight $\omega_i = 1$ citepGauss-Legendre.

The process of CLPT code is in the same way, we evaluate first the different functions that we need to compute the pairwise velocity moment and we perform interpolation to compute the correlation function ξ_r and pairwise velocity moments $V_{12}(\mathbf{r})$ and $\sigma_{12}(\mathbf{r})$. First we evaluate $R_n(k)$ and $Q_n(k)$ functions describ in appendix A using QAG algorithm and Gauss-quadrature with 128 points. Secondly, we compute correlators U_i , A_{ij} and W_{ijk} Eq.(81) by evaluating their scalar functions Eq.(91) to Eq.(108). In the same way, we evaluate operators g_i , G_{ij} and Γ_{ijk} . All integration evaluations use CQUAD algorithm, a doubly-adaptive quadrature routine. Moreover we use gsl matrix tool to perform matrix inversion A with LU decomposition and compute the determinant. Finally to obtain final predictions we evaluate integrals over M_n Eq.(76, 77, 78). To compute integrals over M_n , we make a change of variable $\mathbf{y} = \mathbf{q} - \mathbf{r}$ and we decompose \mathbf{y} on the *los* as explain in §4.1. Therefore, $y_{\perp} = y\sqrt{1 - \mu^2}$ and $y_{\parallel} = y\mu$, where y_{\perp} is the perpendicular component to the *los* and μ is the cosine of the angle θ between the direction of \mathbf{y} and y_{\parallel} the parallel component to the *los*. Thus, we can evaluate the integral in spherical coordinates :

$$\int d^3q M_n(\mathbf{q}, \mathbf{r}) = 2\pi \int dy d\theta y^2 M_n(y) \quad (72)$$

This integrals is performed using a Riemann sum over $d\theta$ for each step of the integral over dq . Riemann sum is an approximation of integral using finite sum,

$$\int f(x)dx \approx \sum_i f(x_i)\Delta x \quad (73)$$

where $\Delta x = x_i - x_{i-1}$. And integral over dq is performed using Gauss quadrature. The output of CLPT prediction are given for each bias component : F_0 , $\langle F' \rangle$, $\langle F'' \rangle$, $\langle F' \rangle^2$, $\langle F'' \rangle^2$ and $\langle F' \rangle \langle F'' \rangle$. Where F_0 is the non biased component. Therefore, $\langle F' \rangle$ and $\langle F'' \rangle$ are free parameters that we called in our code f_1 and f_2 . We fix them before computing the convolution. Different numerical integration techniques had been chosen in order to optimize the rapidity of the code execution and keep a good precision on integral evaluations. We tested a lot of ways to compute each integral and we kept the best time/precision ratio for each.

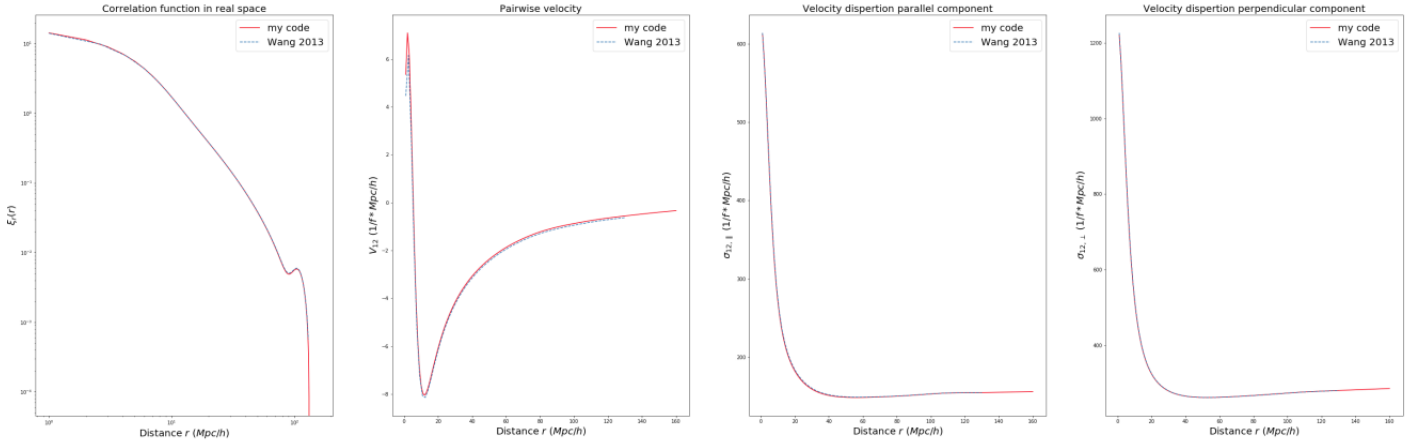


Figure 8: Comparison of CLPT predictions between my code (red line) and the code used in Wang et al. (2014) (blue dashed line).

7.2 Code results

In this part we present the result and the comparison for linear and CLPT prediction. We compare our results with results from Wang et al. (2014). Figure 8 shows the comparison for the same input power spectrum file ($\Omega_M = 0.26479$, $\Omega_\Lambda = 0.73521$, $\sigma_8 = 0.8$ and $h = 0.71$), CLPT predictions for both codes. We find a quasi perfect overlap between both codes for each function. We did the same plot for linear predictions and we found the same alignment. Results of the convolution by the gaussian kernel Eq.47 are shown in figure 9 for CLPT and linear predictions of the real space correlation function ξ_r and both moments of the pairwise velocity function σ_{12} and v_{12} . For both predictions we obtain the squashing effect of Kaiser at large scale. On small scales, linear prediction do not see the feature of finger of god. Whereas, with CLPT predictions, we see both features, fingers of God at small scales $s < 10 h^{-1}$ Mpc and squashing effect at large scale. However at large scales, we should recover the linear theory of Kaiser describes in §4.2 and therefore the contours for both predictions should overlap on large scales. Figure 10 shows contours of $\chi^2_s(s_{||}, s_{\perp})$ evaluated at the same values. We see that CLPT (solid line) and linear (dashed line) contours does not overlap on large scales. Therefore, we underlie a problem in the code that might come from the evaluation of the convolution because predictions for both model are well-evaluated according to Reid & White (2011) (see Figure 8). We compare also the multipoles $\xi_0(s)$, $\xi_2(s)$, $\xi_4(s)$ in Figure 11. Figure 11 display the comparison between multipoles from the linear prediction of Kaiser (solid line), and Gaussian streaming model for linear prediction (dashed line) and CLPT predictions (dot line). The first monopole predictions for the 3 models in red are almost overlapping at intermediate scales ($10 < s < 70 h^{-1}$) Mpc. While at large scale, the BAO bump is smoothed for CLPT predictions.

This results is not suprising because non-linearities in velocity field tend to smoothed the BAO peak. However the quadrupole $\xi_2(s)$, from statistics predicted by CLPT and the GSM is much smaller than the linear prediction for both Kaiser and GS models. Reid & White (2011) notices a difference of 5% on intermediate between the model and their N-Body simulation results. However, our prediction from CLPT moments is much higher than 5%. Quadrupoles are the most sensitive to the convolution, since the anistropies from peculiar velocities are imprint in. Therefore, the shift, between linear and CLPT predictions might be come from the wrong convolution evaluation. The hexadecapole does not give information since it is very small for the 3 predictions.

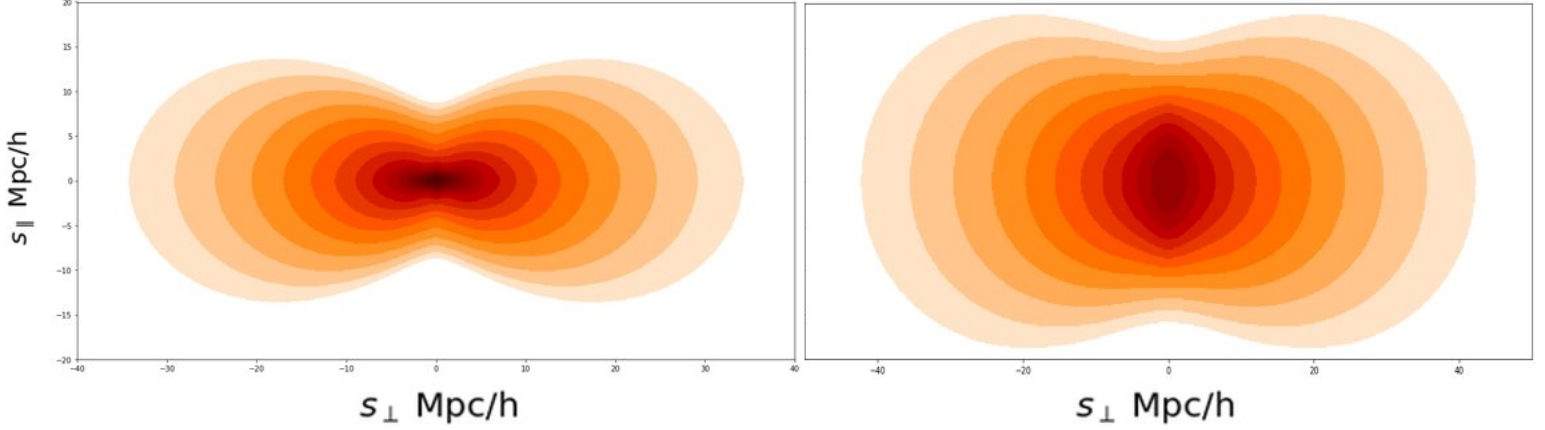


Figure 9: Contour plots that compare theoretical predictions from linear predictions (*left panel*) and CLTP predictions (*right panel*). The x-axis goes from -40 to 40 $h^{-1}\text{Mpc}$ and y-axis from -20 to 20 $h^{-1}\text{Mpc}$

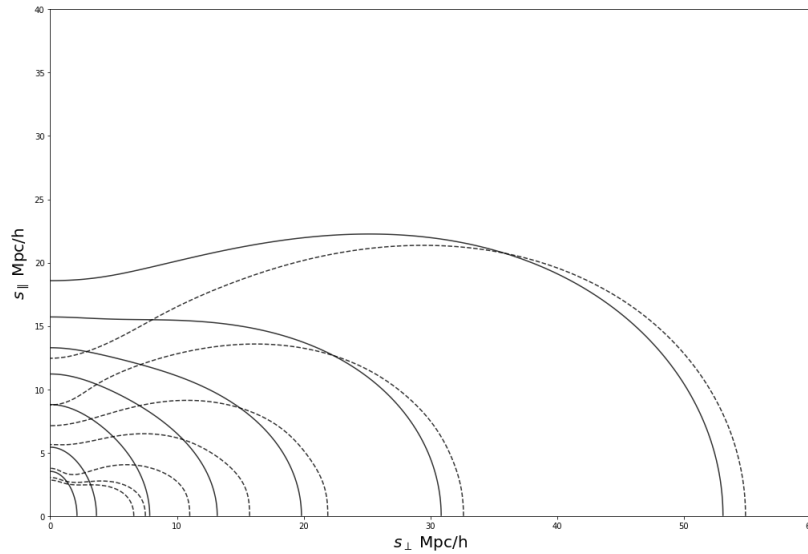


Figure 10: Contour plots of CLPT (solid line) and linear (dashed line) 2-PCF in redshift space.

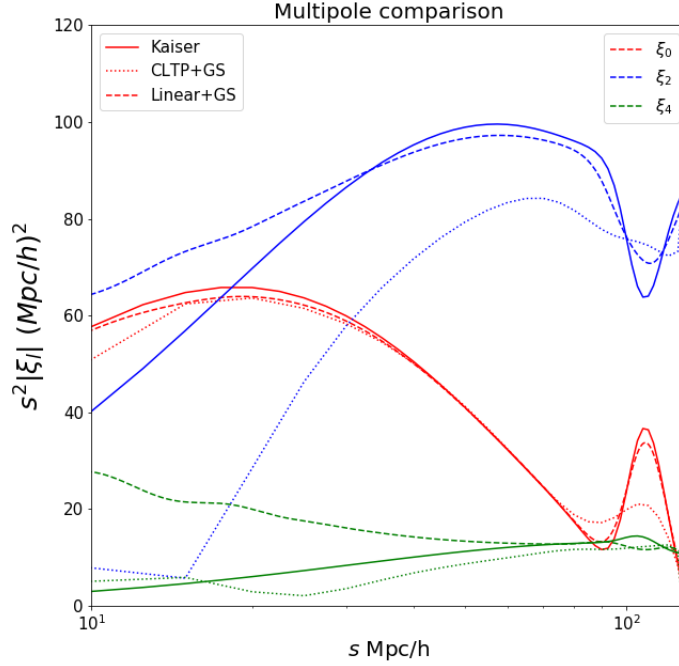


Figure 11: This plot display the monopole $\xi_0(s)$ (red lines), the quadrupole $\xi_2(s)$ (blue lines) and the hexadecapole $\xi_4(s)$ (green line) for Gaussian streaming model with linear statistics (dashed lines) and CLPT statistics (dotted lines) and Kaiser model (solid lines).

8 Simulation

8.1 Comparison Simulation-GS+CLPT model

To assess the accuracy of our analytic model we compare it to DM halo correlation functions derived from N-body simulations UNIT (Chuang et al. 2019). The simulation is of a Λ -CDM cosmology with cosmological parameters taken from the Table 4 of Planck Collaboration et al. (2016) with $\Omega_m = 0.3089$, $h \equiv H_0/100 = 0.6774$, and $\sigma_8 = 0.8147$. The box size is $1000 h^{-1}\text{Mpc}$ and the simulations start at $a \equiv 1/(1+z) = 0.01$ ($z = 99$). The number of dark matter particles is 40963, which correspond to a particle mass of $1.2 \times 10^9 h^{-1} M_{\text{sun}}$. From the simulation, we want to measured the halo 2-PCF. There are many estimators in the literature to measure the 2-PCF. In our work we used the Landy-Szalay estimator to measured the 2-PCF from simulations (Landy & Szalay 1993):

$$\xi(r) = \frac{DD(r) - 2DR(r) + RR(r)}{RR(r)} \quad (74)$$

$DD(r)$ represent pairs of galaxy or halo in the data set, $RR(r)$ are the random pairs taking from a random catalogue and $DR(r)$ are the data-random cross-pairs separated distance by distance r . This estimator is often used to measure 2-PCF in simulations or data sets because it present a minimum root mean square compared to other estimators. To avoid border effect in galaxy surveys, the random catalogue have to be at least 10 times greater than the data set. We compute the correlation function and the multipole with a tree algorithm to compute the pair DD , DR and RR . We use a sample of 1 400 000 haloes in a mass bin between 12.5 and $13 \log M_{\text{sun}}$ and we generate

a random catalogue of $20 \cdot 10^6$ galaxies in order to have a least random catalogue ten times bigger than the halo sample from the simulations. When we use heavy DM haloes $M_h > 12.5 \log M_{sum}$ as tracer of density field, we expect an higher value of bias parameter $b \approx 1.6$. Indeed, heavy haloes are fewer, and younger than classical DM haloes as a milky-way like DM halo $11 \log M_{sum}$ consequently, they less represent the real density field. We use fiducial value from the simulation to fix the value of the growth rate $f(z) = \Omega_M(z)^{0.55} =$ with $\Omega_M(z)$ given by :

$$\Omega_M(z) = \frac{\Omega_{M,0}(1+z)^3}{\Omega_{M,0}(1+z)^3 + \Omega_{\Lambda,0}} \quad (75)$$

Here the simulation results are at redshift $z = 0$, so $f = 0.521324$. In order to compare our model with simulations results we have to determine first, the bias factor b from the simulation sample. To do so, we treat $\langle F' \rangle$, $\langle F'' \rangle$ as free parameters in our model and fit them to the real-space correlation function, $\xi(r)$, measured in the N-body simulations by the Landy-Szalay parameter (Eq.74). Top-left panel of Figure 12 shows the real-space 2-PCF in the simulation sample (in blue) and the best fit from GSM using CLPT statistics. We find lagrangian bias value of $\langle F' \rangle = 0.48$ and $\langle F'' \rangle = 0.05$. The fitting was perform using a brute force over $\langle F' \rangle$ and $\langle F'' \rangle$ between $[0, 2]$. Then, using these values of bias parameter we compare the both monopole and quadrupole in redshift-space. The quadrupole in real space is obviously zero because the quadrupole trace anisotropies. Since we do not take in account peculiar velocities we do not have a quadrupole in the 2-PCF. Figure 12 shows the same pattern for the monopole and the quadrupole for the GSM with CLPT predictions than we see in §7.2, we under estimates both multipoles at intermediate scales. Wang et al. (2014) provide accurate results over N-Body simulations and shows that the CLPT and the Gaussian streaming model provide a good agreement with simulation results at scales $< 5h^{-1}\text{Mpc}$.

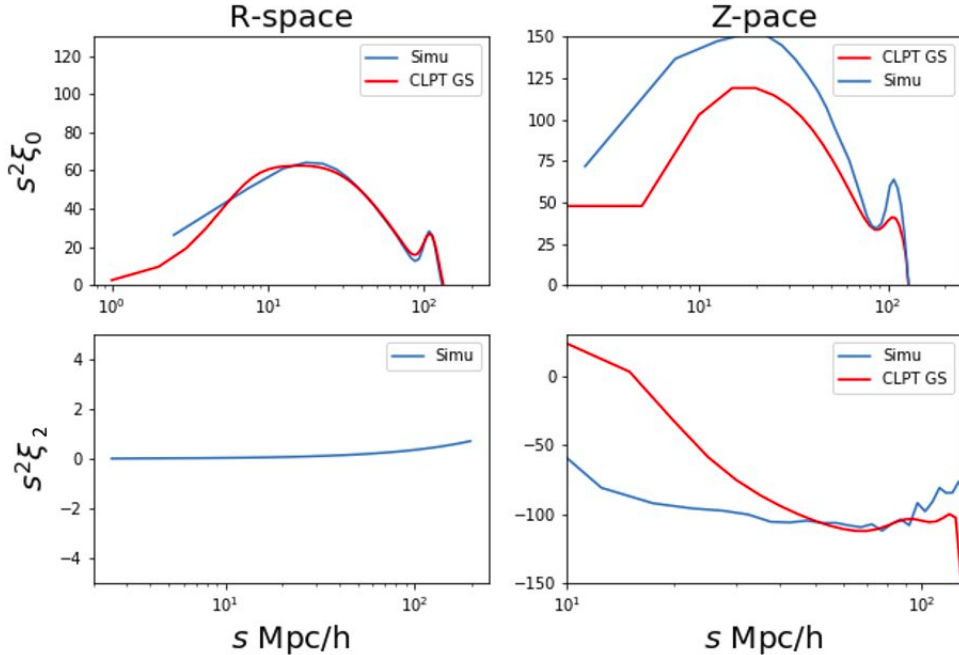


Figure 12: Comparison of real-space (*left panels*) and redshift-space (*right panels*) of the monopole $\xi_0(s)$ (*upper panels*) and the quadrupole $\xi_2(s)$ measured from the simulation (*blue line*) and predict by CLTP statistics with the GSM (*red line*). Y-axis unit is $(h^{-1}\text{Mpc})^2$.

9 Conclusion

Redshift space distortion can be used to discriminate between different models of gravity by measuring the growth rate $f(z)$ on cosmological structures and helped to understand the accelerating expansion of the Universe. We have investigate the applicability to modelling redshift-space distortions through the Gaussian Streaming Model of Fisher (1995) using CLPT statistics to evaluate the moments of the pairwise velocity probability distribution function. In particular we have develop a C code to compute and predict the 2 points correlation function and these multipoles. Unfortunately, results from this are not correct yet. The next improvement of the code will be to fix the problem with the convolution in the GSM. Future prospect of this work can be to compare the Eulerian perturbation theory of RSD from Taruya et al. (2010) and the Lagrangian perturbation theory. Moreover in the next few years, we expect a wealth of new observations with the space surveys Euclid. These observations will provide high-precision measurements of the growth of structure which will allow us to achieve statistical errors of about 1%. These measurements will strongly constrain the dark energy and the expansion history of the Universe over the past ~ 10 billion years. Therefore, the improvement of RSD models is a key ingredient to extract cosmological information from these surveys.

A CLPT functions

In this appendix we define the relevant functions that are used in the CLPT from Carlson et al. (2013) and Wang et al. (2014).

We define M_0 , $M_{1,n}$ and $M_{2,nm}$ from equations 67 :

$$M_0 = \frac{1}{(2\pi)^{3/2}|A|^{1/2}} e^{-\frac{1}{2}(\mathbf{r}-\mathbf{q})^T \mathbf{A}^{-1}(\mathbf{r}-\mathbf{q})} \times \left\{ 1 + \langle F' \rangle^2 \xi_R - 2 \langle F' \rangle U_i g_i + \frac{1}{2} \langle F'' \rangle^2 \xi_R - 2 \langle F' \rangle \langle F'' \rangle \xi_R U_i g_i \right. \\ \left. - [\langle F'' \rangle + \langle F' \rangle^2] U_i U_j G_{ij} + \frac{1}{6} W_{ijk} \Gamma_{ijk} - \langle F' \rangle A_{ij}^{10} G_{ij} - \langle F'' \rangle U_i^{20} g_i - \langle F' \rangle^2 U_i^{11} g_i + O(P_L^3) \right\} \quad (76)$$

$$M_{1,n} = \frac{f^2}{(2\pi)^{3/2}|A|^{1/2}} e^{-\frac{1}{2}(\mathbf{r}-\mathbf{q})^T \mathbf{A}^{-1}(\mathbf{r}-\mathbf{q})} \times \left\{ 2 \langle F' \rangle \dot{U}_n - g_i \dot{A}_{in} + \langle F'' \rangle \dot{U}_n^{20} + \langle F' \rangle^2 \dot{U}_n^{11} + 2 \langle F' \rangle \langle F'' \rangle \xi_L \dot{U}_n \right. \\ \left. - 2 \langle F' \rangle g_i \dot{A}_{in}^{10} - \frac{1}{2} G_{ij} \dot{W}_{ijn} - 2 [\langle F'' \rangle + \langle F' \rangle^2] g_i U_i \dot{U}_n - \langle F' \rangle^2 \xi_L g_i \dot{A}_{in} - 2 \langle F' \rangle G_{ij} U_i \dot{A}_{in} + O(P_L^3) \right\} \quad (77)$$

$$M_{2,nm} = \frac{f^2}{(2\pi)^{3/2}|A|^{1/2}} e^{-\frac{1}{2}(\mathbf{r}-\mathbf{q})^T \mathbf{A}^{-1}(\mathbf{r}-\mathbf{q})} \times \left\{ 2 [\langle F' \rangle^2 + \langle F'' \rangle] \dot{U}_n \dot{U}_m - 2 \langle F' \rangle (\dot{A}_{in} g_i \dot{U}_m + \dot{A}_{im} g_i \dot{U}_n) \right. \\ \left. - \dot{A}_{im} \dot{A}_{jn} G_{ij} + [1 + \langle F' \rangle^2 \xi_L - 2 \langle F' \rangle U_i g_i] \ddot{A}_{nm} + 2 \langle F' \rangle \ddot{A}_{nm}^{10} - \ddot{W}_{inm} g_i + O(P_L^3) \right\} \quad (78)$$

$\langle F^{(n)} \rangle$ is the expectation value of the n th derivative of $F(\delta_R)$.

$$\int \frac{d\lambda}{2\pi} \tilde{F}(\lambda) \exp^{\frac{1}{2} \lambda^2 \sigma_R^2} (i\lambda)^n = \langle F^{(n)} \rangle, \quad (79)$$

The local Lagrangian bias is fully characterized by a series of these parameters $\langle F^{(n)} \rangle$, which we call local Lagrangian bias parameters. Therefore, in our case the local Lagrangian bias is well defined with the 2 first derivatives : $\langle F' \rangle, \langle F'' \rangle$.

The operator g_i , G_{ij} , Γ_{ijk} are defined as:

$$g_i = (A^{-1})_{ij} (q_j - r_j), \quad G_{ij} = (A^{-1})_{ij} - g_i g_j, \\ \Gamma_{ijk} = (A^{-1})_{ij} g_k + (A^{-1})_{ki} g_j + (A^{-1})_{jk} g_i - g_i g_j g_k. \quad (80)$$

We define the cumulant $\langle \delta_1^m \delta_2^n \Delta_{i_1} \dots \Delta_{i_r} \rangle_c$ called "Lagrangian correlators" by Carlson et al. (2013) based on their tensor rank r . For $r = 0$, since δ_R is Gaussian, the only non-vanishing cumulants are:

$$\langle \delta_1^2 \rangle_c = \langle \delta_2^2 \rangle_c \equiv \sigma_R^2, \quad (81)$$

$$\langle \delta_1 \delta_2 \rangle_c \equiv \xi_R(\mathbf{q}). \quad (82)$$

For $r = 1, 2$, and 3 we denote U_i^{mn} , A_{ij}^{mn} and W_{ijk}^{mn} :

$$U_i^{mn(p)} = \langle \delta_1^m \delta_2^n \Delta_i^{(p)} \rangle_c, \quad A_{ij}^{mn(pq)} = \langle \delta_1^m \delta_2^n \Delta_i^{(p)} \Delta_j^{(q)} \rangle_c \\ W_{ijk}^{mn(pqr)} = \langle \delta_1^m \delta_2^n \Delta_i^{(p)} \Delta_j^{(q)} \Delta_k^{(r)} \rangle_c, \quad (83)$$

The LPT expansion of the field $\vec{\Delta}$ has the form:

$$\vec{\Delta} = \vec{\Delta}^{(1)} + \vec{\Delta}^{(2)} + \vec{\Delta}^{(3)} + \dots, \quad (84)$$

If we expand the velocity fields for the correlator we get (up to order $O(P_L^2)$):

$$\begin{aligned} U_i &= U_i^{(1)} + U_i^{(3)} + \dots, \quad U_i^{20} = U_i^{20(2)} + \dots, \quad U_i^{11} = U_i^{11(2)} + \dots, \\ A_{ij} &= A_{ij}^{(11)} + A_{ij}^{(22)} + A_{ij}^{(13)} + A_{ij}^{(31)} + \dots, \quad A_{ij}^{10} = A_{ij}^{10(12)} + A_{ij}^{10(21)} + \dots, \\ W_{ijk} &= W_{ijk}^{(112)} + W_{ijk}^{(121)} + W_{ijk}^{(211)} + \dots. \end{aligned} \quad (85)$$

Similarly, we have for $M_{1,n}$:

$$\begin{aligned} \dot{U}_n &= \frac{\langle \delta_1 \dot{\Delta}_n \rangle}{f} = U_n^{(1)} + 3U_n^{(3)} + \dots, \quad \dot{U}_n^{20} = \frac{\langle \delta_1^2 \dot{\Delta}_n \rangle}{f} = U_n^{20(2)} + \dots, \quad \dot{U}_n^{11} = \frac{\langle \delta_1 \delta_2 \dot{\Delta}_n \rangle}{f} = U_n^{11(2)} + \dots, \\ \dot{A}_{in} &= \frac{\langle \Delta_i \dot{\Delta}_n \rangle}{f} = A_{in}^{(11)} + 3A_{in}^{(13)} + A_{in}^{(31)} + 2A_{in}^{(22)} + \dots, \quad \dot{A}_{in}^{10} = \frac{\langle \delta_1 \Delta_i \dot{\Delta}_n \rangle}{f} = 2A_{in}^{10(12)} + A_{in}^{10(21)} + \dots, \\ \dot{W}_{ijn} &= \frac{\langle \delta_1 \Delta_i \Delta_j \dot{\Delta}_n \rangle}{f} = 2W_{ijn}^{(112)} + W_{ijn}^{(121)} + W_{ijn}^{(211)} + \dots. \end{aligned} \quad (86)$$

And $M_{2,nm}$:

$$\begin{aligned} \ddot{A}_{nm} &= \frac{\langle \dot{\Delta}_n \dot{\Delta}_m \rangle}{f^2} = A_{nm}^{(11)} + 3A_{nm}^{(13)} + 3A_{nm}^{(31)} + 4A_{nm}^{(22)}, \\ \ddot{A}_{10,nm} &= \frac{\langle \delta_1 \dot{\Delta}_n \dot{\Delta}_m \rangle}{f^2} = 2A_{nm}^{10(12)} + 2A_{nm}^{10(21)}, \\ \ddot{W}_{inm} &= \frac{\langle \delta_1 \Delta_i \dot{\Delta}_n \dot{\Delta}_m \rangle}{f^2} = 2W_{inm}^{(112)} + 2W_{inm}^{(121)} + W_{inm}^{(211)}. \end{aligned} \quad (87)$$

By translational symmetry, a Lagrangian correlator can only depend on the Lagrangian separation $\mathbf{q} = \mathbf{q}_2 - \mathbf{q}_1$, therefore correlators must be of the form (Annexe B1 from Carlson et al. (2013)):

$$U_i(\mathbf{q}) = U(q) \hat{q}_i \quad (88)$$

$$A_{ij}(\mathbf{q}) = X(q) \delta_{ij} + Y(q) \hat{q}_i \hat{q}_j \quad (89)$$

$$W_{ijk}(\mathbf{q}) = V_1(q) \hat{q}_i \delta_{jk} + V_2(q) \hat{q}_j \delta_{ki} + V_3(q) \hat{q}_k \delta_{ij} + T(q) \hat{q}_i \hat{q}_j \hat{q}_k \quad (90)$$

Evaluating the Lagrangian correlators reduces to computing a set of scalar functions of q define by Carlson et al. (2013) :

$$\xi_L(q) = \frac{1}{2\pi^2} \int_0^\infty dk \, k^2 P_L(k) j_0(kq) \quad (91)$$

$$V_1^{(112)}(q) = \frac{1}{2\pi^2} \int_0^\infty \frac{dk}{k} \left(-\frac{3}{7} \right) R_1(k) j_1(kq) \quad (92)$$

$$V_3^{(112)}(q) = \frac{1}{2\pi^2} \int_0^\infty \frac{dk}{k} \left(-\frac{3}{7} \right) Q_1(k) j_1(kq) \quad (93)$$

$$S^{(112)}(q) = \frac{1}{2\pi^2} \int_0^\infty \frac{dk}{k} \frac{3}{7} [2R_1(k) + 4R_2(k) + Q_1(k) + 2Q_2(k)] \frac{j_2(kq)}{kq} \quad (94)$$

$$T^{(112)}(q) = \frac{1}{2\pi^2} \int_0^\infty \frac{dk}{k} \left(-\frac{3}{7} \right) \times [2R_1 + 4R_2 + Q_1 + 2Q_2] j_3(kq) \quad (95)$$

$$U^{(1)}(q) = \frac{1}{2\pi^2} \int_0^\infty dk \, k \, (-1) P_L(k) j_1(kq) \quad (96)$$

$$U^{(3)}(q) = \frac{1}{2\pi^2} \int_0^\infty dk \, k \, \left(-\frac{5}{21}\right) R_1(k) j_1(kq) \quad (97)$$

$$U_{20}^{(2)}(q) = \frac{1}{2\pi^2} \int_0^\infty dk \, k \, \left(-\frac{3}{7}\right) Q_8(k) j_1(kq) \quad (98)$$

$$U_{11}^{(2)}(q) = \frac{1}{2\pi^2} \int_0^\infty dk \, k \, \left(-\frac{6}{7}\right) [R_1(k) + R_2(k)] j_1(kq) \quad (99)$$

$$X_{10}^{(12)}(q) = \frac{1}{2\pi^2} \int_0^\infty dk \, \frac{1}{14} \left\{ 2[R_1(k) - R_2(k)] + 3R_1(k) j_0(kq) \right. \quad (100)$$

$$\left. -3[3R_1(k) + 4R_2(k) + 2Q_5(k)] \frac{j_1(kq)}{kq} \right\} \quad (101)$$

$$Y_{10}^{(12)}(q) = \frac{1}{2\pi^2} \int_0^\infty dk \, \left(-\frac{3}{14}\right) [3R_1(k) + 4R_2(k) + 2Q_5(k)] \times \left[j_0(kq) - 3 \frac{j_1(kq)}{kq} \right] \quad (102)$$

$$X^{(11)}(q) = \frac{1}{2\pi^2} \int_0^\infty dk \, P_L(k) \left[\frac{2}{3} - 2 \frac{j_1(kq)}{kq} \right] \quad (103)$$

$$X^{(22)}(q) = \frac{1}{2\pi^2} \int_0^\infty dk \, \frac{9}{98} Q_1(k) \left[\frac{2}{3} - 2 \frac{j_1(kq)}{kq} \right] \quad (104)$$

$$X^{(13)}(q) = \frac{1}{2\pi^2} \int_0^\infty dk \, \frac{5}{21} R_1(k) \left[\frac{2}{3} - 2 \frac{j_1(kq)}{kq} \right] \quad (105)$$

$$Y^{(11)}(q) = \frac{1}{2\pi^2} \int_0^\infty dk \, P_L(k) \left[-2j_0(kq) + 6 \frac{j_1(kq)}{kq} \right] \quad (106)$$

$$Y^{(22)}(q) = \frac{1}{2\pi^2} \int_0^\infty dk \, \frac{9}{98} Q_1(k) \left[-2j_0(kq) + 6 \frac{j_1(kq)}{kq} \right] \quad (107)$$

$$Y^{(13)}(q) = \frac{1}{2\pi^2} \int_0^\infty dk \, \frac{5}{21} R_1(k) \left[-2j_0(kq) + 6 \frac{j_1(kq)}{kq} \right] \quad (108)$$

$R_n(k)$ et $Q(k)$ functions are defined in Matsubara (2008):

$$R_n(k) = \frac{k^3}{4\pi^2} P_L(k) \int_0^\infty dr \, P_L(kr) \tilde{R}_n(r) \quad (109)$$

and

$$Q_n(k) = \frac{k^3}{4\pi^2} \int_0^\infty dr \, P_L(kr) \int_{-1}^1 dx \, P_L(k\sqrt{y}) Q_n(r, x), \quad (110)$$

where $y(r, x) = 1 + r^2 - 2rx$ and the Q_n are given by :

$$Q_1 = \frac{r^2(1-x^2)^2}{y^2}, \quad Q_2 = \frac{(1-x^2)rx(1-rx)}{y^2},$$

$$Q_5 = \frac{rx(1-x^2)}{y}, \quad Q_8 = \frac{r^2(1-x^2)}{y},$$

and R_n :

$$\tilde{R}_1(r) = \int_{-1}^{+1} dx \, \frac{r^2(1-x^2)^2}{1+r^2-2rx}$$

$$\tilde{R}_2(r) = \int_{-1}^{+1} dx \, \frac{(1-x^2)rx(1-rx)}{1+r^2-2rx}$$

References

- Bernardeau, F., Colombi, S., Gaztañaga, E., & Scoccimarro, R. 2002, *Phys. Rep.*, 367, 1
- Beutler, F., Blake, C., Colless, M., et al. 2012, *MNRAS*, 423, 3430
- Blake, C., Brough, S., Colless, M., et al. 2012, *MNRAS*, 425, 405
- Burbidge, E. M., Burbidge, G. R., Fowler, W. A., & Hoyle, F. 1957, *Reviews of Modern Physics*, 29, 547
- Carlson, J., Reid, B., & White, M. 2013, *MNRAS*, 429, 1674
- Chuang, C.-H., Prada, F., Pellejero-Ibanez, M., et al. 2016, *MNRAS*, 461, 3781
- Chuang, C.-H., Yepes, G., Kitaura, F.-S., et al. 2019, *MNRAS*, 487, 48
- de la Torre, S., Guzzo, L., Peacock, J. A., et al. 2013, *A&A*, 557, A54
- de la Torre, S., Jullo, E., Giocoli, C., et al. 2017, *A&A*, 608, A44
- Dvali, G., Gabadadze, G., & Porrati, M. 2000, *Physics Letters B*, 485, 208
- Fisher, K. B. 1995, *ApJ*, 448, 494
- Galassi, M. e. a. 2018, *GNU Scientific Library Reference Manual*
- Gil-Marín, H., Percival, W. J., Cuesta, A. J., et al. 2016, *MNRAS*, 460, 4210
- Gorski, K. 1988, *ApJ*, 332, L7
- Guzzo, L., Pierleoni, M., Meneux, B., et al. 2008, *Nature*, 451, 541
- Hamilton, A. J. S. 1998, in *Astrophysics and Space Science Library*, Vol. 231, *The Evolving Universe*, ed. D. Hamilton, 185
- Hawken, A. J., Granett, B. R., Iovino, A., et al. 2017, *A&A*, 607, A54
- Howlett, C., Ross, A. J., Samushia, L., Percival, W. J., & Manera, M. 2015, *MNRAS*, 449, 848
- Kaiser, N. 1987, *MNRAS*, 227, 1
- Landy, S. D. & Szalay, A. S. 1993, *ApJ*, 412, 64
- Lewis, A. & Bridle, S. 2002, *Phys. Rev. D*, 66, 103511
- Matsubara, T. 2008, *Phys. Rev. D*, 78, 083519
- Nesseris, S. & Perivolaropoulos, L. 2008, *Phys. Rev. D*, 77, 023504
- Okumura, T., Hikage, C., Totani, T., et al. 2016, *PASJ*, 68, 38
- Peacock, J. A., Cole, S., Norberg, P., et al. 2001, *Nature*, 410, 169
- Peebles, P. J. E. 1980, *The large-scale structure of the universe*
- Penzias, A. A. & Wilson, R. W. 1965, *ApJ*, 142, 419

- Piessens, R., de Doncker-Kapenga, E., & Ueberhuber, C. W. 1983, Quadpack. A subroutine package for automatic integration
- Planck Collaboration, Ade, P. A. R., Aghanim, N., et al. 2014, A&A, 571, A12
- Planck Collaboration, Ade, P. A. R., Aghanim, N., et al. 2016, A&A, 594, A13
- Reid, B. A., Samushia, L., White, M., et al. 2012, MNRAS, 426, 2719
- Reid, B. A. & White, M. 2011, MNRAS, 417, 1913
- Riess, A. G., Macri, L. M., Hoffmann, S. L., et al. 2016, ApJ, 826, 56
- Samushia, L., Percival, W. J., & Raccaanelli, A. 2012, MNRAS, 420, 2102
- Scoccimarro, R. 2004, Phys. Rev. D, 70, 083007
- Taruya, A., Nishimichi, T., & Saito, S. 2010, Phys. Rev. D, 82, 063522
- Wang, L., Reid, B., & White, M. 2014, MNRAS, 437, 588
- Zel'Dovich, Y. B. 1970, A&A, 500, 13